JGR Atmospheres

RESEARCH ARTICLE
10.1029/2024JD042266

Key Points:

- The disturbances exhibit top-heavy upward motion and midlevel vorticity near the vorticity center before the formation of easterly waves (EWs)
- Interaction with the Papagayo jet and enhanced top-heavy upward motion facilitate the tilting of vorticity and formation of EWs
- The weakened and less top-heavy upward motion after the formation of EWs is likely modulated by multiple environmental conditions

Supporting Information:

Supporting Information may be found in the online version of this article.

Correspondence to:

Y. Zhou,
Yihao.Zhou@colostate.edu

Citation:

Zhou, Y., & Maloney, E. D. (2025). Dynamics and energetics associated with two east Pacific easterly waves during the OTREC campaign in August 2019. *Journal of Geophysical Research: Atmospheres*, *130*, e2024JD042266. https://doi.org/10.1029/2024JD042266

Received 20 AUG 2024
Accepted 26 MAR 2025

Dynamics and Energetics Associated With Two East Pacific Easterly Waves During the OTREC Campaign in August 2019

Yihao Zhou[1] and **Eric D. Maloney**[1]

[1]Department of Atmospheric Science, Colorado State University, Fort Collins, CO, USA

Abstract This study investigates the vertical structure and related dynamical and energy conversion processes that aided the development of two east Pacific easterly waves (EWs) during the 2019 OTREC (Organization of Tropical East Pacific Convection) campaign period. The initial mesoscale convective systems (MCSs) that seeded both disturbances formed near the Panama Bight and developed into EWs near the Papagayo jet exit region. In the MCS stage, both disturbances were characterized by top-heavy vertical motions and midlevel vorticity near the maximum vorticity center. The deep convection caused strong latent heating and eddy available potential energy (EAPE) generation and conversion to eddy kinetic energy (EKE) in the upper levels. When the disturbances moved to the south of the Papagayo jet, they interacted with the low-level shear vorticity there, enhancing low-level stretching and vorticity. Subsequently, the top-heavy upward motion intensified and led to enhanced stretching and vorticity intensification at midlevels. The enhanced stretching on the southwest side also favored the formation of southwest-northeast tilted vorticity at midlevels that characterizes EWs. After the EWs formed near the jet exit, the vertical motion weakened and became more bottom-heavy, with the maximum vorticity shifting to lower levels. This change in the vertical motion profile near the jet exit region is likely modulated by the lower sea surface temperature, reduced moisture, and weaker convective instability. While EAPE-to-EKE conversion weakened during this period, the low-level barotropic conversion of EKE in the jet exit served as the primary energy source for the EWs.

Plain Language Summary Easterly waves (EWs) are important convective systems in the tropical east Pacific and can seed the tropical cyclones. While the vertical motion structure of the system is crucial for the vorticity growth and formation of EWs, its characteristics and related dynamical processes during evolution remain unclear. This study investigates the development of two EW cases in August 2019 during the field project, Organization of Tropical East Pacific Convection, using satellites, field observations, and reanalysis data. We examined the evolution of the vertical motion profile and the systems' interaction with the Papagayo jet, and analyzed how this interaction may impact the vorticity evolution and energy conversion of EWs. We also examined the environmental conditions that affect the vertical motion profile and strength of the disturbances. The results provide useful insights into the development and formation mechanisms of east Pacific EWs, and can serve as a basis for future modeling studies.

1. Introduction

Easterly waves (EWs) are one of the dominant synoptic-scale disturbances in the eastern Pacific basin, and generally feature zonal length scales around 2,000–4,000 km and periods of 3–5 days, with westward phase speeds around 10 m s^{-1} and propagation tracks near the Central American coastline (Serra et al., 2008, 2010; Tai & Ogura, 1987). EWs are most active during boreal summer and autumn and are important components of tropical weather and climate during this season, contributing to the climatological feature of the east Pacific intertropical convergence zone (ITCZ) (e.g., Adames & Ming, 2018; Nitta & Takayabu, 1985; Roundy & Frank, 2004). EWs are commonly coupled to deep convection and can serve as precursors to tropical cyclones in the east Pacific (Avila & Guiney, 2000; Avila et al., 2003; Dunkerton et al., 2009; Molinari & Vollaro, 2000; Pasch et al., 2009; Serra et al., 2010). EWs and associated westward-propagating tropical variability can also produce a large fraction of seasonal rainfall in Central America and Mexico (Dominguez et al., 2020).

The precise origins of east Pacific EWs remain a topic of active investigation. Some previous studies suggest that east Pacific EWs can originate from African EWs, which propagate over the Central American isthmus and strengthen in the east Pacific (Avila & Pasch, 1992; Frank, 1970; Rappaport & Mayfield, 1992; Serra et al., 2008, 2010; Shapiro, 1986; Zehnder et al., 1999). Other studies suggest that EWs can also be generated in the east Pacific through the upscale growth of local disturbances (Ferreira & Schubert, 1997; Maloney & Hartmann, 2001; Nitta & Takayabu, 1985; Serra et al., 2010; Tai & Ogura, 1987; Toma & Webster, 2010a, 2010b), such as the convective systems driven by diurnal variations in the Panama Bight (Rydbeck et al., 2017; Torres et al., 2021; Whitaker & Maloney, 2020). Serra et al. (2010) showed that some east Pacific EWs originate from Atlantic disturbances while others initiate locally in the Caribbean and east Pacific. Rydbeck et al. (2017) suggests that both EWs propagating from West Africa and those initiated locally are important to the number and intensity of EWs and tropical cyclones in the east Pacific. Therefore, the formation and development of east Pacific EWs may be influenced by a complex interplay of remote and local factors.

Compelling evidence exists that the background state of the east Pacific can significantly modulate EW activity. Low-level easterly winds from the Caribbean Sea can cross through the mountain gap near Lake Nicaragua, producing the Papagayo jet in the east Pacific. In boreal summer, a low-level westerly branch of the southwesterly cross-equatorial flow in the east Pacific known as the Choco jet supports moisture transport to the Colombian coast and triggers organized orographic convection there (Jaramillo et al., 2017; Mejía et al., 2021). These background features of winds and jets in the east Pacific have been hypothesized to be important factors modulating the development of EWs. Serra et al. (2010) suggested that the Caribbean low-level jet (CLLJ) and its extension into the east Pacific as the Papagayo jet are a source of energy for EWs, and a stronger CLLJ and Papagayo jet can produce increased numbers of EWs and tropical cyclones in the ITCZ. Fu et al. (2021) indicated that the easterly moisture transport from the Caribbean is important to the seasonal deep convection and tropical cyclone activity in the east Pacific. Rydbeck and Maloney (2014) showed that the background atmospheric state of the east Pacific varies dramatically on intraseasonal timescales, and stronger eddy kinetic energy (EKE) and positive convective anomalies are found during intraseasonal phases with westerly low-level winds than easterly phases. Whitaker and Maloney (2018) investigated the impacts of the Madden-Julian oscillation (MJO) and CLLJ on background winds and EW activity in the east Pacific, and found that easterly CLLJ and MJO phases support EWs development in the ITCZ, while westerly MJO phases are favorable for the EWs development paralleling the Central American coast. The above studies reveal that the characteristics of low-level winds and jets in the east Pacific are important for EW development.

The detailed vertical structure of EWs is also important for their vorticity development and energy exchange with the background state. Rydbeck and Maloney (2015) showed that the low-level vertical stretching induced by convection anomalies preferentially occurring in the southwest and northeast quadrants of EWs can strengthen the low-level vorticity, which supports the horizontal tilting of the wave and favors barotropic conversion from the background cyclonic zonal wind shear near the jet region. Rydbeck et al. (2017) showed that vorticity stretching associated with convective heating plays a dominant role in the amplification of EW intensity. In particular, midlevel vorticity convergence associated with stratiform and deep convective heating profiles is important for vorticity stretching and vorticity enhancement. Whitaker and Maloney (2020) investigated a June 2012 EW case locally generated in the east Pacific with a WRF simulation, and showed that the disturbance is characterized by stratiform structures and a midlevel vortex early in the disturbance life cycle. However, later in its life cycle after the formation of EW, reanalysis indicates the system to be less top-heavy and features stronger low-level vorticity than in WRF, suggesting strong interactions with the Papagayo jet that peaks at low levels. Thus, the vertical structure of east Pacific EWs and their interaction with the background jets during their development are still not well understood. Whitaker and Maloney (2020) suggested that further studies entraining field observations to help interpret EW formation, including those during the 2019 Organization of Tropical East Pacific Convection (OTREC) campaign period, are needed.

Fuchs-Stone et al. (2020) analyzed the overall characteristics of convection during the OTREC period using 3DVAR analysis. Although they did not specifically focus on EWs, they found that developing convective disturbances exhibit mainly bottom-heavy mass flux profiles that favor interaction with the Papagayo jet. Huaman et al. (2021) identified three convectively active EWs during the OTREC period, aiming to investigate the impacts of EWs on the climatological deep and shallow circulations in the east Pacific. Valencia et al. (2024) also investigated the EWs during OTREC, with focus on how convectively coupled EWs traversing over the western Caribbean modulate the Choco low-level jet and precipitation over tropical and northwestern South America. However, these studies did not investigate in detail how EW vertical structure and associated dynamical processes contributed to EW development.

In this study, we will investigate the development process of two EW cases (hereafter EW1 and EW2) during the OTREC period using satellite and reanalysis data and field observations. These two EWs occurred around August 8 and 16 in 2019, respectively, and were both documented by Huaman et al. (2021) and Valencia et al. (2024) using different identification methods. We will focus on the following questions: (a) How do vertical profiles of convection and vertical velocity evolve during the development of the EWs? (b) How do variations in the systems' vertical motion profiles and interactions with the jet impact the evolution of vorticity and energetics? (c) How do variations in the background environment affect the vertical profiles of the system? Section 2 describes the data sets used in this study. Section 3 presents the overview of the two EW cases. Section 4 presents the vertical and horizontal evolution of vertical motion and vorticity in developing disturbances. Section 5 and 6 analyze the vorticity and EKE budgets, respectively, to understand how vertical structure variations and interactions with the Papagayo jet impact EWs evolution. Section 7 examines the environmental conditions regulating EWs convection and vertical motion. Section 8 gives a summary and some discussions.

2. Data Sets

We used satellite, reanalysis, and field observations to investigate the initiation and development processes of EW1 and EW2 during August 2019 (as described below). The 0.1° × 0.1° observational precipitation product with 0.5-hourly interval from Integrated Multi-satellitE Retrievals for Global Precipitation Mission (IMERG) version 7 (Huffman et al., 2023) is used to show the spatial evolution of precipitation during these two events. The 1-hourly ERA5 data set (Hersbach et al., 2023) with horizontal grid spacing of 0.25° × 0.25° is used to investigate the dynamical structure of EWs (e.g., vertical velocity amd relative vorticity) and provide large-scale environmental fields (e.g., horizontal winds and water vapor).

We also used field observations during the OTREC campaign to validate several variables in ERA5 reanalysis, and to provide further insights for the development of EWs. During the OTREC period, 22 research flights (127 research flight hours) were conducted from 5 August to 3 October 2019 using the NSF/NCAR Gulfstream V aircraft, during which data from 648 dropsondes were collected (Fuchs-Stone et al., 2020). Each flight started approximately at 12 UTC and lasted 6 hr, including deployment of about 32 dropsondes from altitudes near 13 km to the surface. We examined dropsonde profiles of temperature, moisture, and wind fields on August 7 and 16 during the development stages of EW1 and EW2, respectively, to compare to ERA5 reanalysis. The detailed time periods and spatial coverage of dropsondes will be described in Section 4. In addition, the Geostationary Operational Environmental Satellite 16 (GOES-16) images from longwave infrared channel 14 with 6 km × 6 km horizontal resolution were also used as a reference to document the development stage of the EWs. This satellite data set was processed by National Center for Atmospheric Research/Earth Observing Laboratory (NCAR/EOL), and the images are derived from https://catalog.eol.ucar.edu/maps/otrec.

3. Overview of EW Cases

Figure 1 shows Hovmöller diagrams of precipitation and midtroposphere relative vorticity for the two EW events during August 2019, which were diagnosed to produce the strongest precipitation in the OTREC region on August 7 and 15, respectively (Huaman et al., 2021). The initial disturbances of EW1 and EW2 in the Panama Bight have the most prominent vorticity at 500 hPa and 600 hPa, respectively, making these levels the most suitable for subsequent vorticity tracking analyses. Therefore, Figure 1 shows the 500-hPa vorticity for EW1 and the 600-hPa vorticity for EW2.

Precipitation and vorticity in EW1 initiated around 78°W at 06 UTC on August 6, and then propagated westward to 95°W at 12 UTC on August 8. The precipitation subsequently weakened and dissipated, while the vorticity maintained its strength and continued to propagate at the same speed until about August 10. The precipitation and vorticity were generally colocated during propagation, with an overall speed of ∼9.7 m/s (shown by the dashed line in Figure 1a), although the westward propagation speed of precipitation appeared to be slightly faster than that of vorticity. The slightly faster propagation speed of precipitation than vorticity can also be found in the case study of Whitaker and Maloney (2020) (their Figure 3a).

Precipitation and vorticity fields in EW2 are noisier, and the propagation process is not as smooth as that of EW1. The disturbance of EW2 initiated around 78°W at 06 UTC on August 15, but the subsequent propagating precipitation and vorticity disturbances were not as strongly colocated as for EW1. The westward propagation speed of precipitation seems much faster than that of vorticity. Later, we will show that EW2's development from the

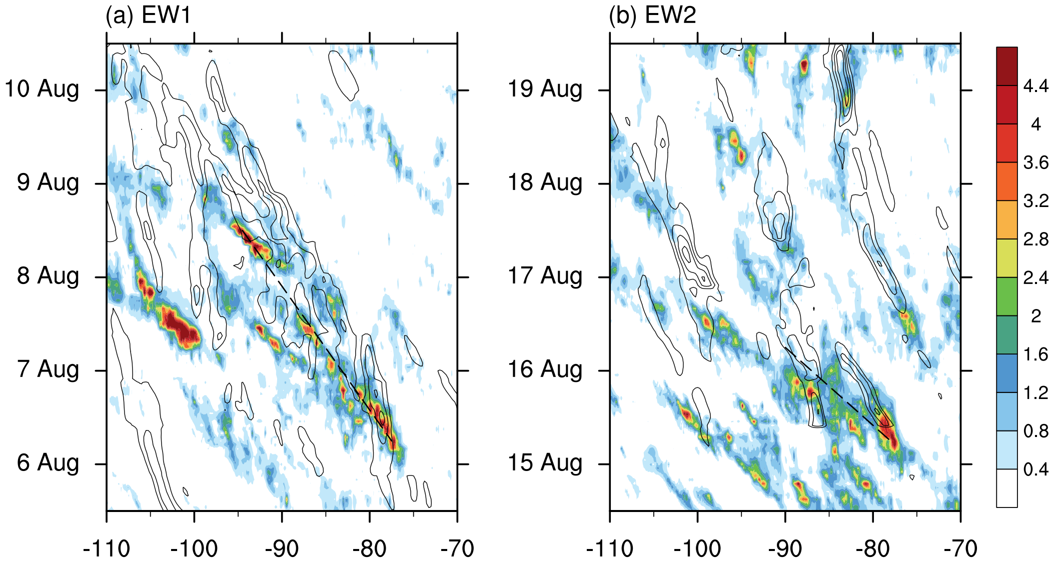

Figure 1. Hovmöller diagrams of the 3°–15°N averaged IMERG precipitation rate (shadings; mm h^{-1}) and ERA5 relative vorticity (contours; s^{-1}; from 1×10^{-5} to 5×10^{-5} s^{-1} by 1×10^{-5} s^{-1}) for (a) EW1 (vorticity at 500 hPa) and (b) EW2 (vorticity at 600 hPa). Dashed lines indicate the approximate propagation path of the system.

mesoscale convective system (MCS) to EW was relatively rapid due to merging with other convective systems, and the distribution of precipitation and vorticity during its development was noisier. The initial disturbance in Panama Bight weakened during its merger with the disturbance in the Caribbean, while a new vorticity center developed to its west, leading to the seemingly unsmooth propagation of vorticity. Therefore, the Hovmöller diagram may not comprehensively depict the propagation process of the EW2 disturbance. The propagation speed of EW2 between 78°W and 90°W was approximately 15.5 m/s.

Figure 2 show horizontal maps of the evolution of precipitation and 500-hPa winds and vorticity for EW1. Convection and vorticity began to form near the Colombian coast about 00 UTC on August 6, and the initiation of convective system can also be found in the GOES-16 satellite image (Figure S1a in Supporting Information S1). The convection intensified and became better organized in the Panama Bight around 06 UTC (Figure S1b in Supporting Information S1), with an appearing MCS and precipitation significantly increasing. The vorticity also subsequently strengthened, coupled with the enhanced precipitation that covered much of the Panama Bight (Figures 2c and 2d). The precipitation of disturbance in the early stage is located slightly south of the vorticity center, consistent with the findings of previous studies (e.g., Rydbeck et al., 2017). The midlevel winds in the Panama Bight and the adjacent western ocean were weak northeasterly. On August 7 (Figures 2e–2h), the vorticity and precipitation gradually propagated westward to near the western coast of Costa Rica. The vorticity range expanded and generally exhibited a west-northwest horizontal orientation, with easterly winds on its eastern side gradually strengthening. The vorticity continued to strengthen on August 8, and developed a southwest-northeast tilted structure in the Papagayo jet region at 06 UTC (Figure 2j), consistent with the typical EW structure in previous studies (e.g., Raymond et al., 2015; Serra et al., 2008; Whitaker & Maloney, 2020). Therefore, we consider this the time at which the disturbance developed from an MCS into an EW. Strong precipitation reappeared to the northwest of the EW vorticity center. Afterward, the winds at the jet exit and its southern side transitioned to strong southeasterly, and the EW maintained its southwest-northeast tilted structure and continued to propagate northwestward.

The spatial evolution of precipitation and 600-hPa vorticity in EW2 are shown in Figure 3. We use a 3-hr interval here because the MCS-to-EW transition period in EW2 was shorter. During 00 and 03 UTC on August 15, precipitation and vorticity signals appeared near the Colombian coast, with strong easterly flow in this region (Figures 3a and 3b). The initial disturbance significantly intensified around 06 UTC, consistent with the occurrence of organized convective clusters in satellite imagery (Figure S2c in Supporting Information S1), suggesting the formation of an MCS. Precipitation also appeared in the Caribbean north of the MCS, which significantly intensified around 09 UTC, and propagated westward together with the MCS (Figure 3d).

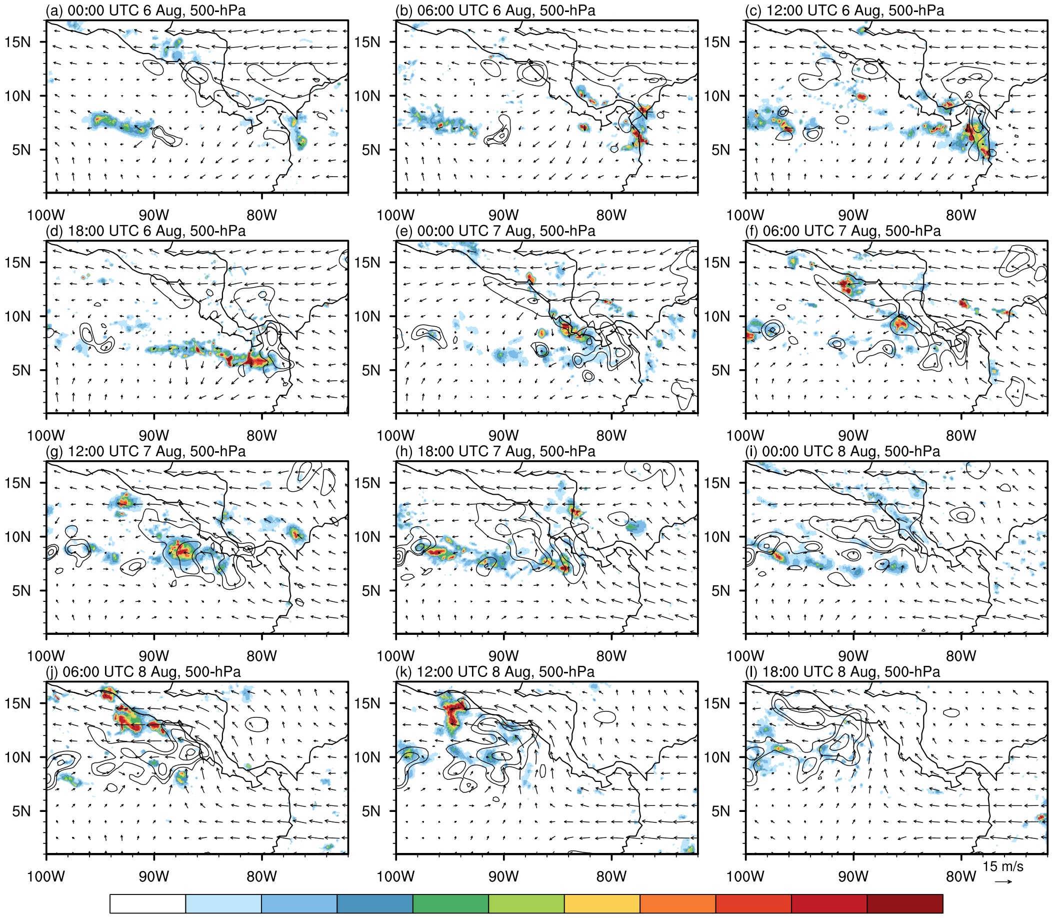

Figure 2. Spatial evolutions of the IMERG precipitation rate (shadings; mm h^{-1}), ERA5 500-hPa winds (vectors; m s^{-1}), and relative vorticity (contours; s^{-1}) for EW1 from 00 UTC 6 August to 18 UTC 8 August with a 6-hourly interval. Vorticity contours are plotted for 2.5, 5, 10, 15, 25, 45, and 65 × 10^{-5} s^{-1}.

Additionally, oceanic convective systems were present to the west of the MCS and gradually intensified. The vorticity associated with the MCS in Panama Bight intensified during 12 and 15 UTC, and then expanded northward and merged with the convective system in the Caribbean. The merged disturbance propagated westward across Central America and subsequently merged with the oceanic system to its west, forming a large-scale vorticity center extending from Panama Bight to Papagayo jet region during 18 and 21 UTC (Figures 3g and 3h). This was accompanied by weakened precipitation over land and increased precipitation to the southwest over the ocean, with the maximum primarily located southeast of the wave trough. The system developed a southwest-northeast tilted vorticity structure near the jet exit around 03 UTC on August 16, suggesting the formation of an EW. During this period, the southeasterly winds gradually strengthened on the southern side, similar to EW1. Afterward, precipitation weakened near the vorticity center, and the EW continued to propagate northwestward with a tilted feature (Figures 3k and 3l).

The subsequent horizontal evolution of EW1 and EW2 is shown in Figures S3 and S4 in Supporting Information S1, respectively. Both EWs continued to propagate northwestward along the North American coastline and developed closed vorticity contours with a near-circular shape around the Gulf of Tehuantepec, accompanied by a strengthening of vorticity. Combining the subsequent vorticity evolution of EW1 and EW2 with the tropical cyclone track map shown in Figure S5 in Supporting Information S1, it is shown that EW1 and EW2 eventually developed into tropical storms Henriette and Ivo on August 12 and 21, respectively. However, the development and transition of these EWs into tropical cyclones during their mature stages are beyond the scope of this study. In the later analysis, we will mainly focus on the evolution of the disturbances and related processes during the MCS stage until shortly after the formation of EWs. In general, the MCS stage in EW1 was from 06 UTC on August 6 to

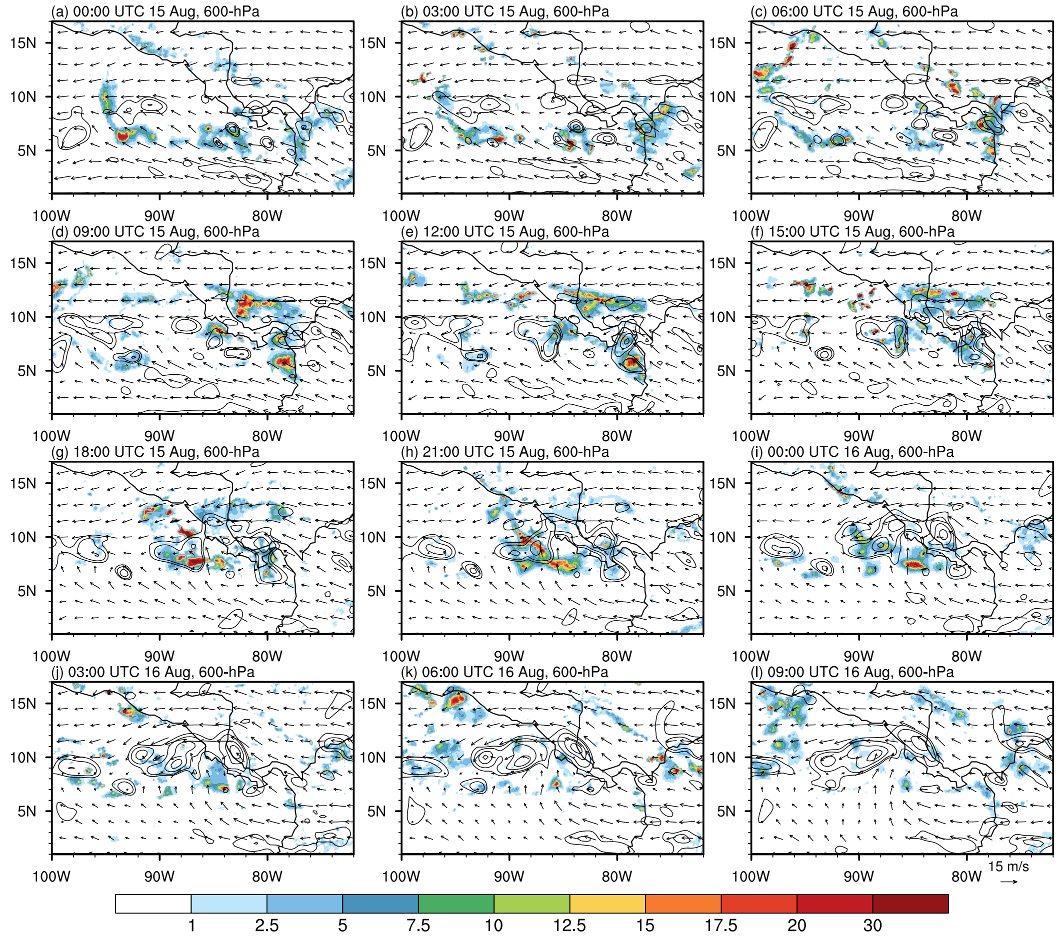

Figure 3. Same as in Figure 2 but for the precipitation rate, 600-hPa winds and relative vorticity of EW2 from 00 UTC 15 August to 09 UTC 16 August with a 3-hourly interval.

06 UTC on August 8, and for EW2, it was from 06 UTC on August 15 to 03 UTC on August 16, followed by their EW stage.

4. Evolution of Vertical Structure

4.1. Vorticity Tracking

To study the vertical structure of EW1 and EW2 during their development, we first defined the vorticity center of the disturbances. Figures 2 and 3 and Figures S1 and S2 in Supporting Information S1 show that the initial convection and vorticity of EW1 and EW2 disturbances formed near the Colombian coast around 00 UTC on August 6 and 15, respectively. Therefore, we limited the identification of the initial vorticity to the area (0–12°N, 79°–73°W), as indicated by the purple boxes in Figures 4a and 4b. The strongest unsmoothed vorticity value within this area was identified as the initial vorticity center. The initial vorticity center of EW1 remains unchanged with a slight modification of the identification area, while that of EW2 shifts to the ocean west of the Colombian coast when the area expanded westward. However, this shift is influenced by the presence of other oceanic convective systems on the western side, and cannot represent the location of EW2 disturbance. Therefore, the selected initial area shown in Figures 4a and 4b appears reasonable. In the subsequent vorticity tracking, the vorticity center at each time step (with a 1-hourly interval) is determined as the location with the maximum unsmoothed vorticity value within a 4° × 4° box centered on the previous vorticity center. Finally, we applied a five-point running average to the obtained 1-hourly vorticity centers to obtain smoother EWs propagation paths. The red dots in Figures 4a and 4b show the resultant 1-hourly vorticity centers for EW1 from 00 UTC on August 6

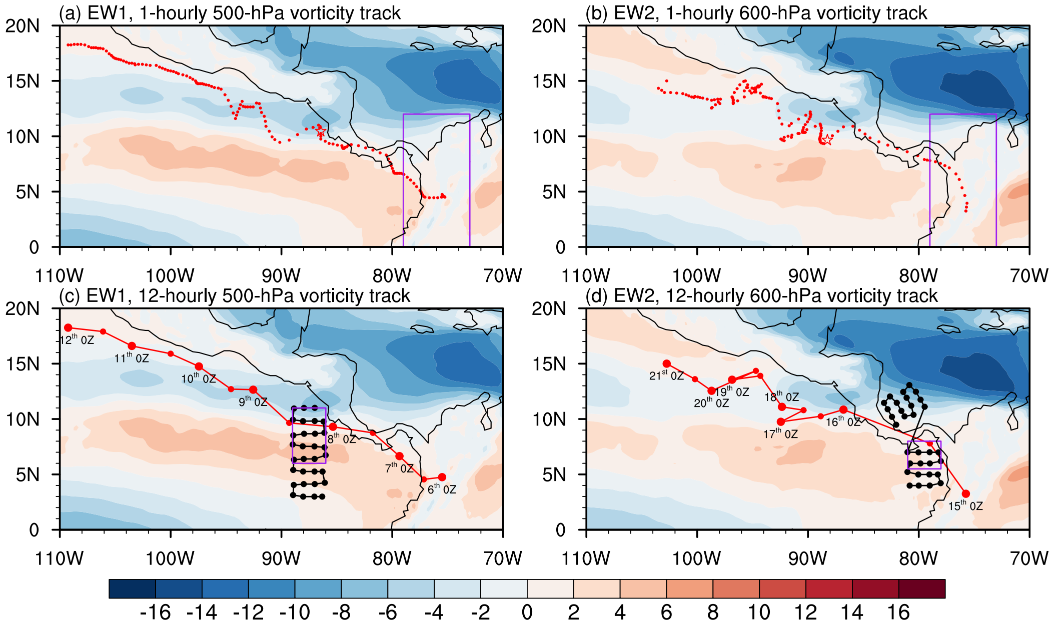

Figure 4. (a) 1-hourly ERA5 500-hPa unsmoothed vorticity maximum locations (red dots) for EW1 from 00 UTC 6 August, with the ERA5 925-hPa total zonal wind (shadings; m s^{-1}, positive and negative values represent westerly and easterly winds, respectively) averaged during August 6–9. (b) Similar to (a) but for 600-hPa vorticity center locations in EW2 from 00 UTC 15 August, and the zonal wind is averaged during August 15–18. The star symbols in panels (a) and (b) denote the location where the easterly wave formed. The purple boxes in panels (a) and (b) indicate the identification region for the initial vorticity center. The red dots in panels (c) and (d) are same as in panels (a) and (b) but for 12-hourly locations, and the red lines indicate the propagation path from east to west. The black dots in panels (c) and (d) denote the locations of flight dropsondes on August 7 and 16, respectively, and the black lines denote the flight paths. The purple boxes in panels (c) and (d) indicate the averaging region used for comparison between ERA5 reanalysis and flight dropsondes.

and for EW2 from 00 UTC on August 15, respectively. The red dots and red lines in Figures 4c and 4d show the 12-hourly vorticity centers sampled from the 1-hourly results for EW1 and EW2 and their paths.

The initial disturbances of EW1 and EW2 near the Colombian coast were probably related to diurnally driven convective systems (Mapes et al., 2003). Subsequently, the disturbances propagated northwestward, developing into EWs near the Papagayo jet exit (roughly 9°–13°N, 86°–89°W, where the strong low-level easterlies predominate as shown in Figure 4), and then propagated to the ocean region southwest of the Mexican coast around August 9. The track of EW2 vorticity was more complex. It merged with disturbances to the north and west on August 15 and reached the jet exit more rapidly (also see Figure 3). It then lingered longer to the west of the jet exit, and finally neared the Mexico coast between August 18 and 19.

It is worth noting that the vorticity centers of EW1 and EW2 are more erratic in the Papagayo jet exit region. This is likely because the spatial range of the vorticity was broader after the EWs formed, with two vorticity maxima evolving asymmetrically on the southwest and northeast sides along the wave axis. We will show the dynamical processes related to the evolution of vorticity intensity and structure in Section 5. Overall, the identified tracks for EW1 and EW2 successfully represent, in a general sense, the main active regions of their large-scale vorticity.

4.2. Vertical Profiles

Before using the vorticity tracks in Figure 4 to analyze the vertical profiles of EW1 and EW2, we used OTREC dropsondes to verify the vertical profiles in ERA5 reanalysis. The black dots in Figures 4c and 4d show the locations of the observations from the flights closest in date to the development of EW1 and EW2, which were conducted on August 7 for the east Pacific and on August 16 for Colombian and the Caribbean, respectively. Figures 4c and 4d shows that the vorticity center of EW1 reached the corresponding aircraft observation area on August 8 (later than the observation), while the vorticity center of EW2 passed the aircraft observation area on August 15 (earlier than the observation). Although the EW1 and EW2 disturbances did not exactly coincide with the timing and location of observations from these two flights, comparing area-averaged ERA5 results with the

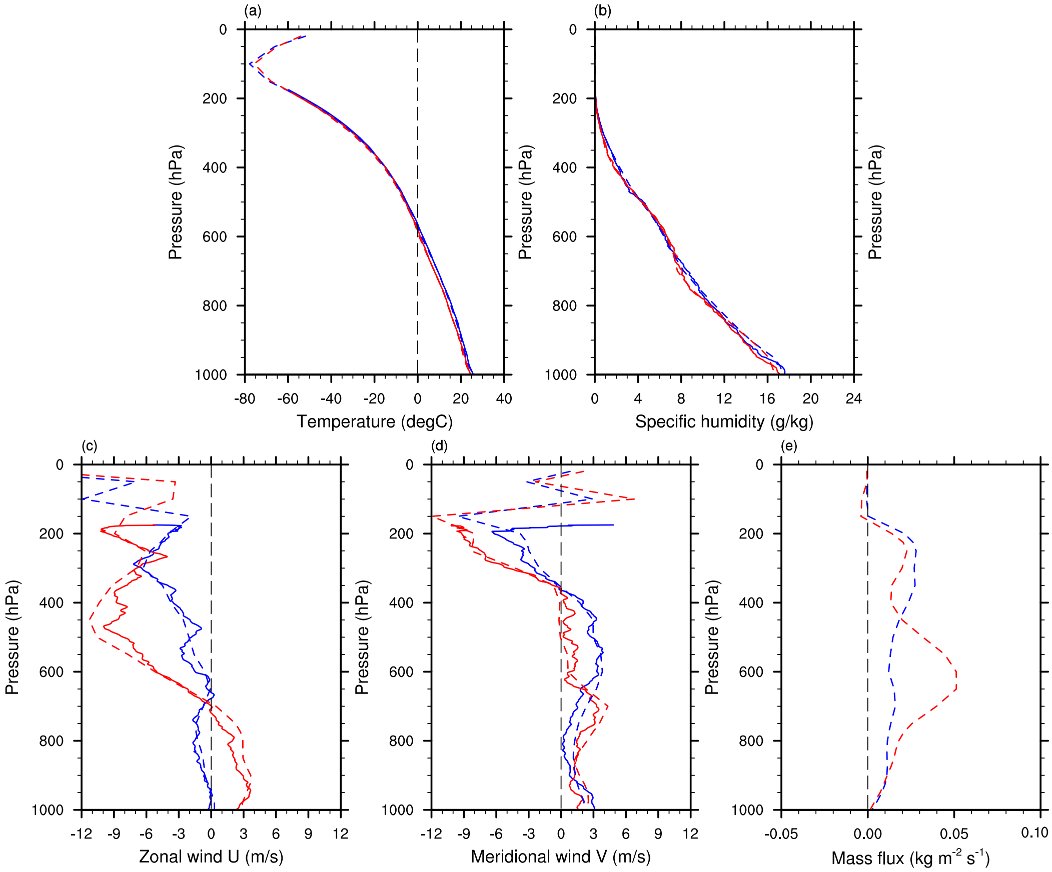

Figure 5. Vertical profiles of (a) temperature (°C), (b) specific humidity (g kg^{-1}), (c) zonal wind (m s^{-1}), (d) meridional wind (m s^{-1}), and (e) mass flux (kg m^{-2} s^{-1}) for the convective cases on August 7 (blue) and 16 (red). Thick and dashed lines represent results from flight dropsondes and ERA5, respectively.

dropsonde array for the convective events occurring near the propagation paths of EW1 and EW2 might still provide useful insights into how well ERA5 represents mesoscale or synoptic-scale disturbances associated with EWs.

Referencing the OTREC convective events selected by Fuchs-Stone et al. (2020) (see their Table 1), the east Pacific convective event on August 7 occurred within the region (6°–11°N, 89°–86°W) around 15–18 UTC, and the convective event near the Colombian coast on August 16 occurred within the region (5.5°–8°N, 81°–78°W) around 14–16 UTC. Figure 5 shows the regional averaged vertical profiles of temperature, humidity, and horizontal winds in ERA5 reanalysis and flight dropsondes for these two convective cases, and mass flux from ERA5. Vömel et al. (2021) indicated that the vertical velocity in dropsondes is estimated based on the difference in the fall rate between observation and the model, which is unreliable for fast-fall sondes. The authors suggest that it is more reasonable to use this vertical velocity estimate to identify the areas of updraft and downdraft above its uncertainty limit (~1 m/s). The vertical velocity from dropsondes indeed exhibits strong oscillations with height and has a significantly greater overall amplitude than the vertical velocity in ERA5 (not shown), which appears to be incorrect. Therefore, we only show the vertical profiles of mass flux from ERA5 in Figure 5f.

The mass flux profiles in the convective events on August 7 and 16 exhibit top-heavy and bottom-heavy features, respectively, consistent with the results based on 3DVAR in Fuchs-Stone et al. (2020) (see their Figure 4), indicating that ERA5 can reasonably represent the degree of top-heaviness of vertical motion. The performance of ERA5 in representing temperature, moisture, and horizontal winds compared to observations is assessed, with results shown in Table S1. The amplitude and the vertical profile of temperature and moisture in ERA5 are in good agreement with observations. While horizontal winds in ERA5 exhibit a larger bias percentage of about 20%–30%, their root mean square deviation is generally less than 1 m/s, with a high vertical correlation coefficient

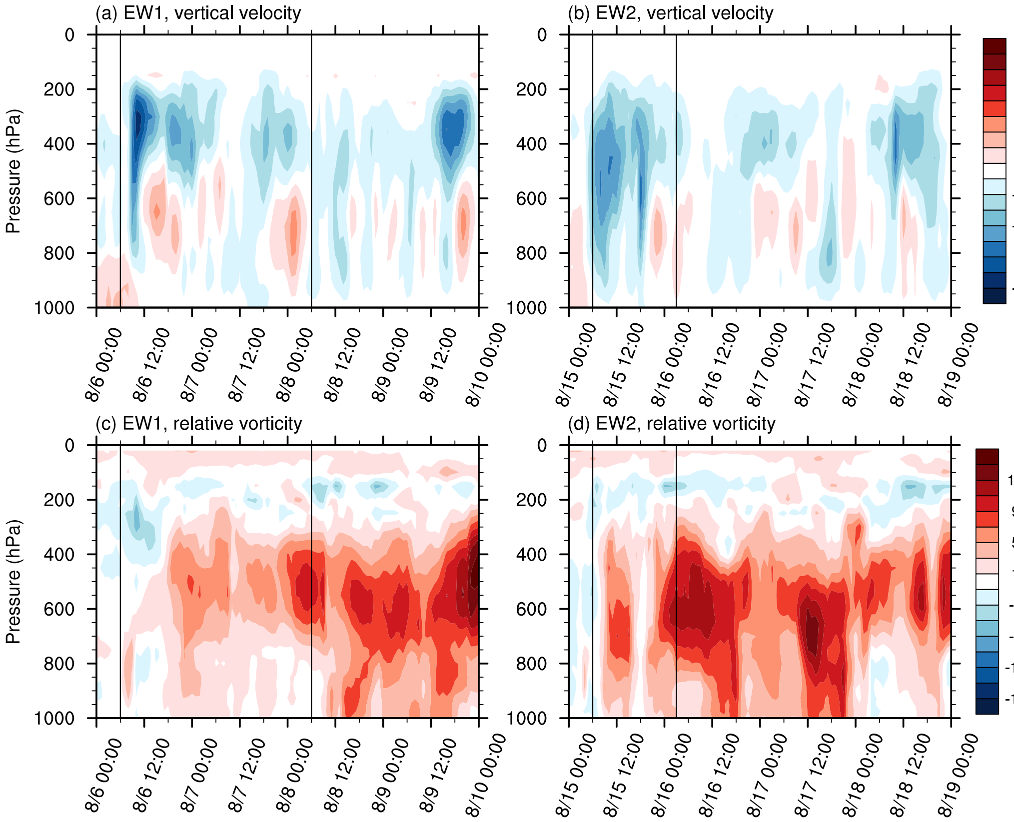

Figure 6. Time-height diagrams of (a) vertical velocity (Pa s^{-1}) and (c) relative vorticity (s^{-1}) averaged across a 2° × 2° box centered on the 1-hourly 500-hPa vorticity maximum locations for EW1 from 00 UTC 6 August. (b) And (d) are same as in panels (a) and (c) but for EW2 results based on its 600-hPa vorticity maximum locations from 00 UTC 15 August. The two black lines in each panel indicate the times of mesoscale convective system and easterly wave formation, respectively.

(around 97%–98%) with observations. This suggests that although ERA5 exhibits some amplitude bias in wind fields, it can well represent their vertical profiles. Therefore, ERA5 adequately captures the vertical structure of the disturbances in EW1 and EW2 along their propagation paths from the Panama Bight to the Papagayo jet exit. We will next use ERA5 reanalysis to study the three-dimensional evolution and related dynamical processes of EW1 and EW2 disturbances. We also note that enhanced local soundings on adjacent land surfaces of Colombia and Costa Rica were conducted during most of the OTREC period to better constrain reanalysis, providing further confidence in reanalysis fields during this time (Wiggins et al., 2023).

Figure 6 shows the evolution of the vertical velocity and relative vorticity structure averaged near the vorticity centers of EW1 and EW2 (the results are not sensitive to the averaging area). After the MCS formed, the vertical velocity in both EW1 and EW2 exhibited a top-heavy profile, with enhanced midlevel vorticity appearing slightly later. During the MCS stage, the maximum upward motion for EW1 is located around 300–400 hPa, and the maximum vorticity is around 500–600 hPa; for EW2, the maximum upward motion is around 400–500 hPa, and the maximum vorticity is around 700 hPa. These results suggest that the formation and maintenance of midlevel vorticity in the MCS stage may be related to midlevel convergence caused by top-heavy vertical motion.

Before the formation of EWs, the top-heavy upward motion in EW1 and EW2 became more pronounced around 00 UTC on August 8 and 16, respectively, showing a stratiform profile with upward motion at upper levels and downward motion at lower levels. When EWs formed near the Papagayo jet exit, there was a significant increase in midlevel vorticity, with the maximum vorticity for both EW1 and EW2 located at 500–600 hPa. After the formation of EWs, the vertical velocity was weaker and exhibited a bottom-heavy or less top-heavy profile, accompanied by the maximum vorticity shifting to lower altitudes (around 600–700 hPa), and the vorticity below 700 hPa also strengthened compared to the MCS stage. As EWs continued to propagate northwestward and moved away from the jet region, upward motion significantly intensified and became top-heavy again around 15

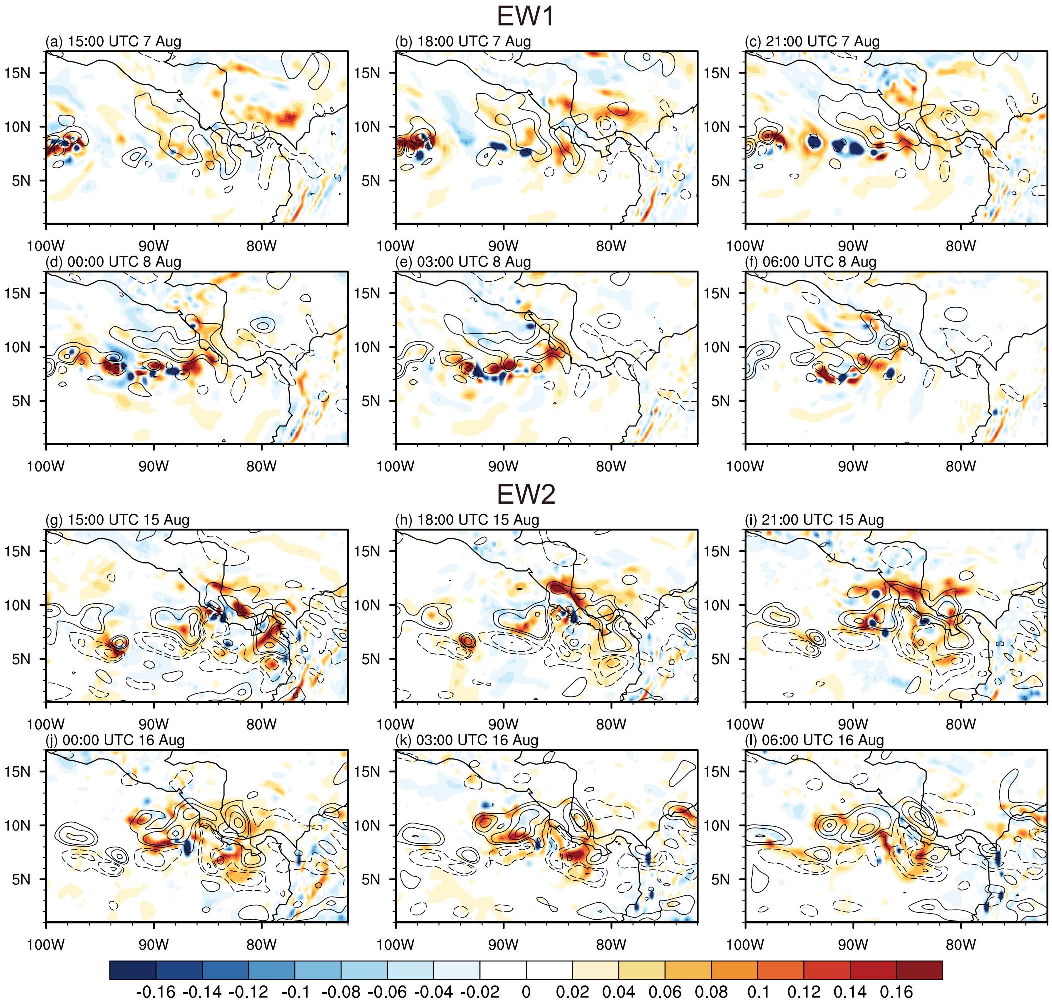

Figure 7. Spatial evolution of ERA5 MFLUXDIF (kg m^{-2} s^{-1}) for (a)–(f) EW1 from 15 UTC 7 August to 06 UTC 8 August with a 3-hourly interval and (g)–(l) EW2 from 15 UTC 15 August to 06 UTC 16 August with a 3-hourly interval. Relative vorticity (contours; s^{-1}) at 500 hPa (600-hPa) for EW1 (EW2) is also shown. Vorticity contours are plotted for 2.5, 5, 10, 15, 25, 45, and 65 × 10^{-5} s^{-1}.

UTC on August 9 for EW1 and 06 UTC on August 18 for EW2. Meanwhile, the maximum vorticity rose back to 500–600 hPa and strengthened significantly.

The above results are similar to the case study of Whitaker and Maloney (2020), who also found that vertical motion exhibited a top-heavy profile in both reanalysis and simulation before EW formation. The top-heavy feature weakened in reanalysis after EW formation, with intensified low-level vorticity compared to the MCS stage. These findings suggest that the vertical structure of vertical motion may play an important role in the evolution of the EW's vorticity field.

4.3. Spatial Evolution of Top-Heaviness

To investigate the spatial evolution of vertical motion top-heaviness during the MCS-to-EW transition, we examined a variable called MFLUXDIF, defined by the difference between averaged vertical mass flux at high levels (7–9 km) and low levels (3–5 km) (Fuchs-Stone et al., 2020; Raymond & Fuchs-Stone, 2021). Positive values of MFLUXDIF represent top-heavy vertical motion profiles, while negative values represent bottom-heavy profiles.

Figure 7 shows the spatial evolution of MFLUXDIF from ERA5 for EW1 and EW2 before and during the formation of the EWs. For EW1, the MFLUXDIF near the vorticity center was positive and increased during 18 and

21 UTC on August 7, and strong negative values appeared to the southwest of the vorticity center. Before EW1 formation, the positive MFLUXDIF continued to strengthen, while the negative values in the southwest decayed and turned positive (Figures 7d and 7e). This was accompanied by a significant enhancement of vorticity in the southwest, which changed the spatial structure of midlevel vorticity and facilitated the presence of southwest-northeast tilted shape. After the EW1 formed at 06 UTC on August 8, the positive MFLUXDIF weakened, consistent with the reduced top-heaviness shown in Figure 6a. These results indicate that a significant enhancement of top-heavy vertical motion preceded the vorticity intensification and EW formation, highlighting the importance of the vertical motion profile in the development of the disturbance.

The evolution of MFLUXDIF with the vorticity in EW2 is broadly similar to EW1, with some differences in the active regions. At 15 UTC on August 15, the vorticity center and positive MFLUXDIF were still located in the Panama Bight, and they strengthened as they moved into the Caribbean and its western land area by 18 and 21 UTC. The positive MFLUXDIF over the ocean southwest of the Papagayo jet increased between 00 and 03 UTC on August 16 (Figures 7j and 7k), and the enhanced vorticity in this area merged with that over the land, facilitating formation of a southwest-northeast tilted midlevel vorticity structure.

In general, the positive MFLUXDIF and related top-heavy vertical motion intensified before the formation of EWs, which were collocated with the vorticity center and can impact its spatial structure and intensity. Specifically, the transition of MFLUXDIF from negative to positive on the southwest side of vorticity center in EW1 led to intensified midlevel vorticity in that region, which favored the formation of southwest-northeast tilted structure. This further suggests that top-heavy vertical motion may promote the enhancement of midlevel vorticity and the formation of EWs tilted vorticity through midlevel convergence and vertical stretching, consistent with some previous studies (e.g., Rydbeck et al., 2017). In the next section, we will analyze the vorticity budget to further examine the vorticity growth process related to vertical motion and stretching.

5. Vorticity Budget

To investigate the processes related to vorticity evolution, we conducted a vorticity budget analysis for EW1 at 500 hPa and EW2 at 600 hPa. The vorticity budget terms are not decomposed into a perturbation and background and will be calculated using total fields. The vorticity budget equation can be written as (e.g., Rydbeck et al., 2017; Whitaker & Maloney, 2020) follows:

$$\frac{\partial \zeta_z}{\partial t} = -\left(u\frac{\partial \eta}{\partial x} + v\frac{\partial \eta}{\partial y}\right) + \eta\frac{\partial \omega}{\partial p} + \left[\frac{\partial}{\partial x}\left(-\zeta_u\frac{\omega}{\rho g}\right) + \frac{\partial}{\partial y}\left(-\zeta_v\frac{\omega}{\rho g}\right)\right] + R,$$

where $\zeta_z = (\partial v/\partial x - \partial u/\partial y)$ is the vertical vorticity, u is the zonal wind, v is the meridional wind, $\eta = \zeta_z + f$ is the absolute vorticity, ω is the vertical pressure velocity, p is pressure, ζ_u is the zonal component of vorticity, ζ_v is the meridional component of vorticity, g is the gravitational acceleration, and ρ is the density of air. The vorticity tendency term on the left side represents the local change of vorticity, which results from terms of horizontal advection, vorticity stretching, and tilting shown on the right side, respectively. The rightmost residual term R is the difference between vorticity tendency on the left side and the sum of the first three terms on the right side. Biases in the reanalysis model, inaccuracies created in calculations, and subgrid-scale processes (e.g., boundary layer or cumulus friction) that are not represented in other terms might partly contribute to the residual R. We used the centered finite-differencing method to calculate the differential terms in time and three-dimensional directions, computing each term hourly. Consistent with previous studies on EW vorticity budgets (e.g., Rydbeck & Maloney, 2015; Rydbeck et al., 2017; and Whitaker & Maloney, 2020), we will show that the vorticity stretching term dominates the vorticity intensification of EW disturbances, and we will mainly focus on it.

5.1. Vertical Stretching

Figure 8 shows the spatial evolution of vorticity and the stretching term for EW1 and EW2. For EW1, the stretching west of Costa Rica was weak at 15 UTC on August 7, and began to strengthen by 18 UTC, with large values of stretching broadly collocated with the vorticity center. Subsequently, as the vorticity stretching intensified and extended southward, the vorticity also significantly strengthened and changed its spatial structure. During 00 and 03 UTC on August 8, enhanced stretching and vorticity occurred on the southwest side of the wave

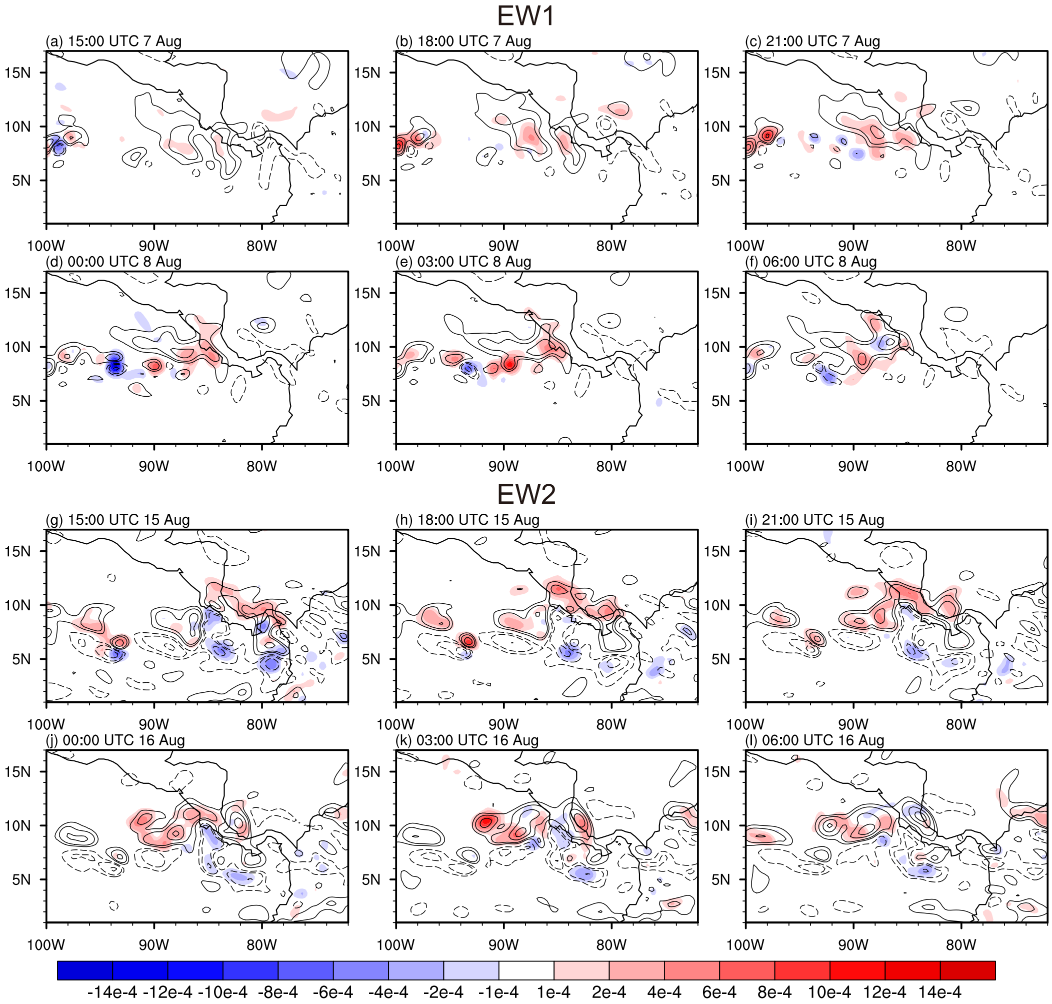

Figure 8. Same as in Figure 7 but for ERA5 vorticity stretching (shadings; s^{-1} day^{-1}) and relative vorticity (contours; s^{-1}) at 500 hPa (600 hPa) for EW1 (EW2).

axis, which coincided with the regions of strong positive MFLUXDIF shown in Figure 7. This resulted in the zonally oriented vorticity gradually transforming into a southwest-northeast tilted structure with increased intensity, facilitating the formation of EW1 around 06 UTC. For EW2, the stretching term was also coupled with the vorticity center and showed significant enhancement before EW formation. From 15 UTC on August 15 to 03 UTC on August 16 (Figures 8g–8k), the evolution of stretching was broadly consistent with the positive values of MFLUXDIF, which both gradually shifted from the Caribbean to the Papagayo jet exit and the ocean to its southwest, resulting in the merger and intensification of the two vorticity centers and the formation of the EW2. During this process, the enhancement of stretching and vorticity over the southwestern ocean is also important for the formation of the tilted vorticity structure.

To further investigate how vertical motion and stretching processes alter the spatial structure of midlevel vorticity, Figure 9 shows the horizontal evolution of the winds, vorticity, and stretching term averaged in the low levels (925–800 hPa). For EW1, the strong meridional shear of zonal wind occurred on the southern side of the Papagayo jet at 15 UTC on August 7 (Figure 9a), resulting in shear vorticity in that region. Holbach and Bourassa (2014) also documented this low-level shear vorticity at the equatorward side of the Papagayo jet and suggested that it can interact with propagating disturbances and favor TC genesis. During 18 and 21 UTC, strong bottom-heavy upward motion appeared southwest of the shear vorticity (as shown by the negative MFLUXDIF values in Figures 7b and 7c), leading to an initial enhancement of stretching and vorticity at low levels (Figures 9b and 9c). During 00 and 03 UTC on August 8, the vorticity developed into the midlevels through vertical stretching

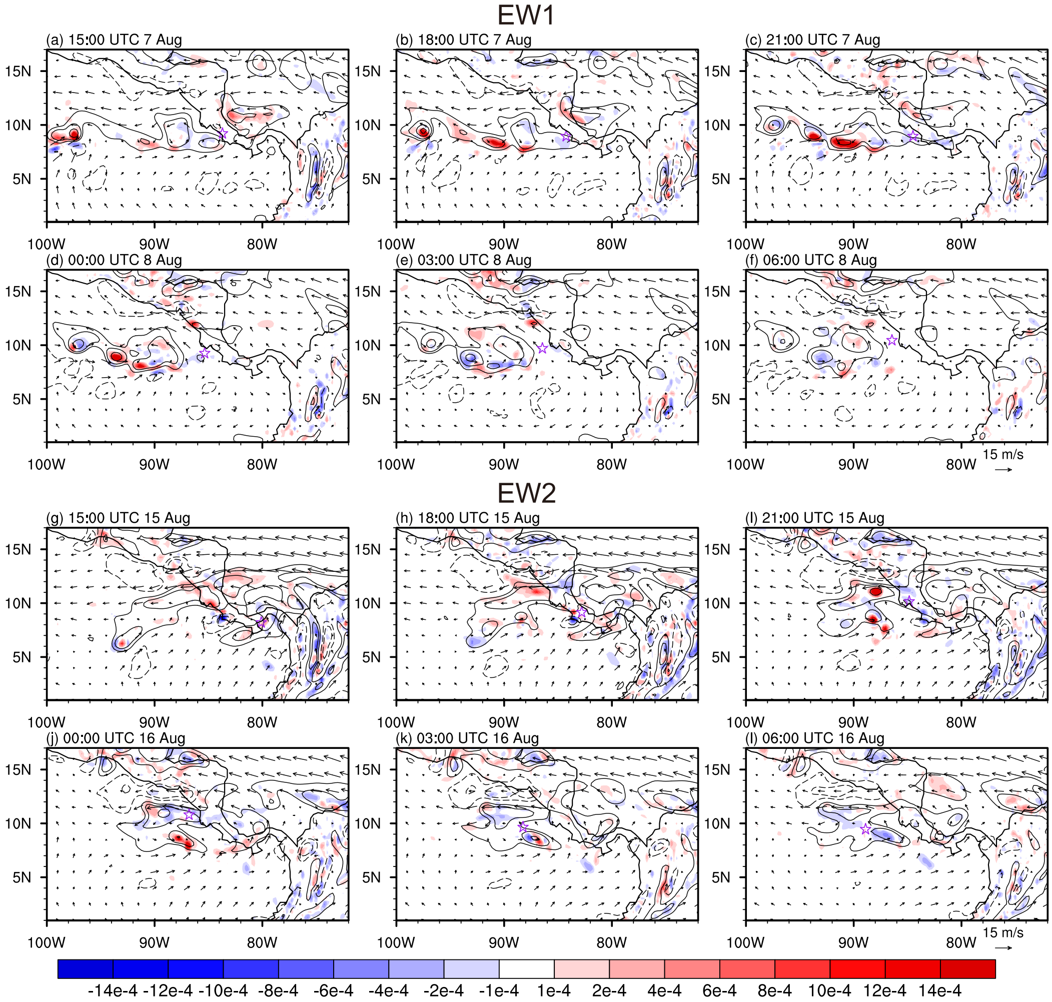

Figure 9. Same as in Figure 8 but for ERA5 vorticity stretching (shadings; s^{-1} day^{-1}) and relative vorticity (contours; s^{-1}) averaged between 925 and 800-hPa for both EW1 and EW2. The averaged wind vectors (m s^{-1}) from 925 to 800 hPa are also plotted. The purple star marks represent the locations of midlevel vorticity maximum (as in Figure 4) at each time.

as top-heavy upward motion strengthened (Figures 7d and 7e). A deep and strong vorticity center from the low to midlevels formed on the southwest side of wave axis, leading to a southwest-northeast tilted structure and the formation of EW1. Such a structure would be expected to grow further in this region through barotropic conversion given background meridional shears of the zonal flow in the jet region (Maloney & Hartmann, 2001; Torres et al., 2021). It is worth noting that before EW1 formation, the maximum midlevel vorticity center of the system (marked by the star symbol in Figure 9) was located east of the low-level shear vorticity, where the low-level vorticity was weak. As the southwestern vorticity continued to strengthen, the midlevel vorticity center shifted to the southwest after EW formation (see Figure 4a), and the low-level vorticity there remained strong (Figure 9f). This explains the strong low-level vorticity that appeared shortly after the formation of EW1 in Figure 6c, which is related to the system's interaction with the low-level jet and wind shear near the jet exit region.

For EW2, the position of the low-level monsoon trough westerlies and shear vorticity is further north, located at the Papagayo jet exit, and there was more noise in the vertical motion and low-level vorticity. The low-level upward motion south of the shear vorticity (the negative MFLUXDIF in Figures 7h–7j) and stretching (Figures 9h–9j) is less evident than in EW1. The southwestern midlevel vorticity was mainly covered by enhanced top-heavy upward motion, leading to the strengthening of midlevel vorticity in that region and the formation of EW's tilted structure. Before EW2 formation, the midlevel vorticity center was located to the east of the low-level shear vorticity, and then shifted to the southwest when EW2 formed (see Figures 4b and 9k), similar to EW1.

Overall, during the MCS-to-EW transition, the midlevel stretching occurred in the vicinity of the vorticity center and significantly intensified it, suggesting its dominant role in the midlevel vorticity enhancement. The stretching term is also important for the evolution of the spatial structure of vorticity and the formation of tilted shape of EW. In addition, the low-level wind shear and vorticity associated with the Papagayo jet may also significantly impact the vorticity evolution, which is particularly evident in EW1. Vorticity can be first enhanced by low-level upward motion in the vicinity, and then develop into the midlevels through vertical stretching induced by the subsequent enhanced top-heavy upward motion before the EW formation, thus leading to midlevel vorticity enhancement and southwest-northeast tilt. This highlights the importance of the vertical motion profile of the system in its interaction with the background jets. The vertically integrated moisture budget results show that there is a positive moisture tendency on the southwest side of wave axis before EW formation, primarily caused by strong vertical moisture advection, with a marginal contribution from horizontal advection (not shown). This moistening related to vertical advection may be one of the reasons for the enhancement of top-heavy upward motion on the southwest side. Rydbeck and Maloney (2015) also indicated that the enhanced moistening southwest of the wave supports convection there, which can induce stretching that is largely in phase with the vorticity and maintains the EW's tilted structure. However, they indicate that the moistening is mainly caused by horizontal advection, with meridional advection primarily resulting from the strong meridional moisture gradient near the ITCZ. Additionally, our results suggest that zonal advection associated with low-level jets (e.g., the Papagayo jet and Choco jet) may also contribute to EW moistening by advecting perturbation moisture. The roles of moisture in the enhancement of upward motion and stretching need to be verified in future research.

5.2. Other Budget Terms

The spatial evolution of the horizontal vorticity advection for EW1 and EW2 is shown in Figure S6 in Supporting Information S1. For both EW1 and EW2, when the vorticity strengthened near the jet exit, positive and negative values of horizontal advection became evident on the northwest and southeast sides of the wave axis, with the latter being stronger, exhibiting an asymmetric feature consistent with that in Whitaker and Maloney (2020). After the formation of EWs, horizontal advection further intensified, which might be partly due to the stronger southeasterly winds on the southeast side, promoting vorticity propagation toward the northwest. Overall, the horizontal advection term acts as the dominant factor controlling the northwestward propagation of the vorticity, and its effect is especially significant after EW formation. However, horizontal advection has a marginal effect on the intensification of vorticity and formation of the EW structure.

The tilting term for EW1 and EW2 (Figure S7 in Supporting Information S1) is weaker than the stretching term and horizontal advection. This term was larger near the Colombian coast and Panama Bight during the early MCS stage, and weakened as the vorticity center propagated away from this region. This is consistent with the conclusions of Rydbeck et al. (2017) and Whitaker and Maloney (2020), who indicated that the large values of the tilting term are confined to land regions and do not continuously propagate, only contributing weakly to the enhancement and propagation of the disturbance during the early MCS stage. Additionally, the residual term (Figure S8 in Supporting Information S1) also showed a smaller effect on vorticity amplitude and propagation than the stretching and horizontal advection terms.

6. Eddy Kinetic Energy Budget

Many previous studies (e.g., Serra et al., 2008, 2010) have indicated that the EKE generated from barotropic and eddy available potential energy (EAPE) conversion play an important role in the formation and development of EWs in the east Pacific. To investigate the EKE maintenance processes during the development of EW1 and EW2, we will conduct an EKE budget analysis. EKE will be defined as (e.g., Rydbeck & Maloney, 2014; Whitaker & Maloney, 2018) follows:

$$K' = \frac{1}{2}\left(\overline{u'^2} + \overline{v'^2}\right),$$

where overbars represent the 11-day running mean and primes represent the deviations from the 11-day running mean. The EKE budget can be written as:

$$\frac{\partial \overline{K'}}{\partial t} = -\overline{V_h} \cdot \nabla_h \overline{K'} - \overline{V'_h \cdot \nabla K'} - \overline{V'_h (V' \cdot \nabla) \overline{V}_h} - \frac{R}{P}\left(\overline{\omega' T'}\right) - \nabla \cdot \left(\overline{V' \Phi'}\right) + D,$$

where V is the three-dimensional wind vector, V_h is the two-dimensional horizontal wind vector, Φ is the geopotential, $R = 287\ \mathrm{J\ kg^{-1}\ K^{-1}}$ is the gas constant for dry air, p is the pressure, ω is the vertical pressure velocity, T is the temperature, and D is the budget residual. The first and second terms on the right side $(-\overline{V_h} \cdot \nabla_h \overline{K'} - \overline{V'_h \cdot \nabla K'})$ represent the advection of EKE by the time mean and perturbation winds, respectively. The third term $(-\overline{V'_h (V' \cdot \nabla) \overline{V}_h})$ represents the barotropic conversion of EKE from the mean kinetic energy. The fourth term $\left(\left(\nabla \cdot \left(\overline{V' \Phi'}\right)\right)\right)$ represents the conversion from EAPE to EKE. The fifth term $\left(\nabla \cdot \left(\overline{V' \Phi'}\right)\right)$ represents the redistribution of EKE by geopotential flux convergence. The residual term D represents the effects of subgrid-scale processes, such as dissipation of EKE by friction, any calculation biases in the budget, and possible effects from analysis increments. The centered finite-differencing method is similarly used to calculate each term, same as in the vorticity budget equation.

Similar to Rydbeck and Maloney (2014), the summer EKE maxima in the east Pacific are primarily located over the Papagayo jet exit region and the ocean to its west (not shown), consistent with the main active regions of EWs during their mature stage and representing the energy of synoptic-scale convective activity associated with EWs. As indicated by previous studies (e.g., Lau & Lau, 1992; Rydbeck & Maloney, 2014), the advection and geopotential flux convergence terms mainly act to redistribute the energy from one location to another, and the real sources or sinks for EKE in the vertical average only include barotropic conversion and EAPE-to-EKE conversion, which are also the leading terms of the EKE budget. We will focus on these two terms in the following analysis.

Figures 10a–10d show the time mean distribution of the 1,000–200-hPa vertically averaged barotropic conversion and EAPE-to-EKE conversion for EW1 and EW2. Large values of barotropic conversion are located near the Papagayo jet exit, with the amplitude in EW1 being stronger than EW2. This term is consistent with influence from the low-level easterly jet and the corresponding strong meridional gradient of the zonal wind in that region (as shown in Figure 4). The EWs both formed near the jet exit where barotropic conversion becomes the primary energy source for the system. Previous studies suggest that the southwest-northeast tilted structure of EWs is favorable for the energy extraction from the meridional shear of the mean zonal wind (e.g., Rydbeck & Maloney, 2015).

Large values of EAPE-to-EKE conversion are located near the Panama Bight, similar to the composite results in Rydbeck and Maloney (2014) and Whitaker and Maloney (2018), which may play an important role in the MCS development. Previous studies indicated that the EAPE generation and subsequent conversion to EKE in the east Pacific are primarily related to the latent heat produced by deep convection (e.g., Rydbeck & Maloney, 2014; Serra et al., 2008, 2010). Therefore, the strong diurnally driven convection in the Panama Bight may facilitate EAPE generation. This term in EW1 is also stronger than that in EW2 especially to the west of the Panama Bight. This difference is likely related to the distinct development paths of EW1 and EW2.

Figures 10e–10h show the vertical evolution of the barotropic and EAPE-to-EKE conversion averaged near the vorticity centers of EW1 and EW2 (the results are not sensitive to the averaging area). During the MCS stage of both EW1 and EW2, barotropic conversion was weak, while EAPE-to-EKE conversion in the upper levels (400–200 hPa) was strong, serving as the main energy source for MCS development. When the EWs formed, the upper-level EAPE-to-EKE conversion weakened while the barotropic conversion in the low levels (below 800 hPa) significantly increased, during which the vorticity center was near the jet exit and the disturbances took on a tilted structure that supported such barotropic conversions. As the EWs then propagated away from the jet exit, the low-level barotropic conversion gradually weakened, and the upper-level EAPE-to-EKE conversion reintensified. Although the EW1 has stronger amplitudes than EW2, the overall evolutions of these two terms are similar for EW1 and EW2. It is worth noting that the amplitude of upper-level EAPE-to-EKE conversion is closely related to the vertical motion profile. This term was stronger when there was strong top-heavy vertical motion, and became weak when the vertical motion weakened or became less top-heavy. This confirms that the EAPE

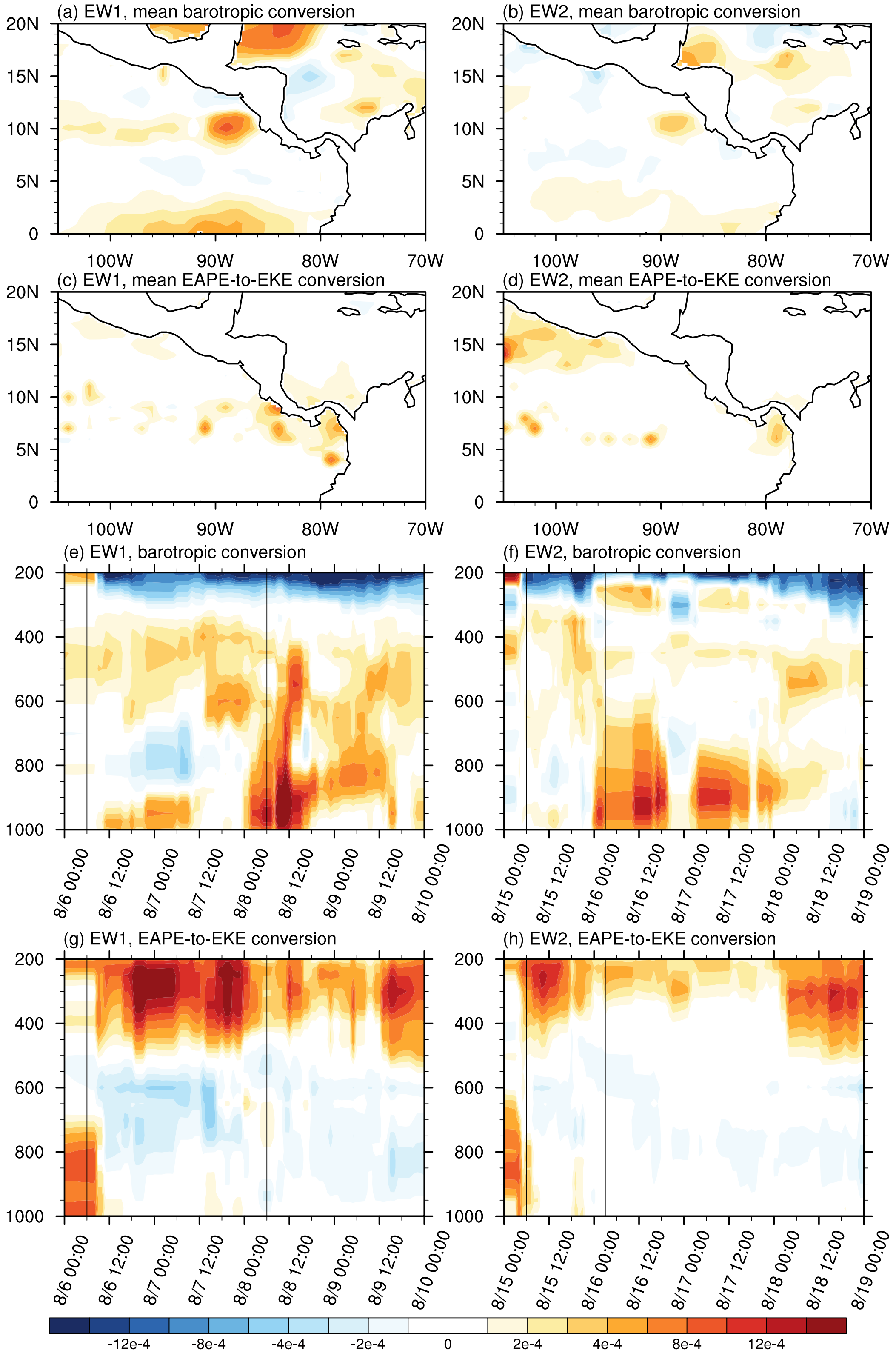

Figure 10. ERA5 vertically averaged (a) barotropic conversion ($m^2\ s^{-3}$) and (c) EAPE-to-EKE conversion from eddy kinetic energy budget for EW1 averaged during 6–9 August. (b) And (d) are same as in panels (a) and (c) but for EW2 averaged during 15–18 August. Time-pressure diagrams of (e) barotropic conversion and (g) EAPE-to-EKE conversion averaged across a 2° × 2° box centered on the 1-hourly 500-hPa vorticity maximum locations for EW1 starting at 00 UTC 6 August. (f) And (h) are same as in panels (e) and (g) but for EW2 results based on its 600-hPa vorticity maximum locations.

generation and conversion to EKE in the east Pacific are primarily associated with upper-level diabatic heating caused by deep convection.

Overall, the roles and impact regions of barotropic and EAPE-to-EKE conversions differ during the development of disturbance. EAPE-to-EKE conversion is more important for the development of MCSs with top-heavy vertical motion. In contrast, barotropic conversion serves as the primary energy source for EWs in the Papagayo jet exit region where the system interacts with the low-level jet, which is discussed when describing Figures 7–9. However, the detailed effects of jet-induced barotropic conversion on EWs near the formation time require further investigation through future numerical simulations, including sensitivity tests that fill topography to remove the jet crossing the Gulf of Papagayo.

7. Effects of Environmental Conditions

In previous results, we found that the vertical structure of vertical motion impacts the evolution of vorticity and EKE conversion during the system development. When EWs formed after disturbances propagated to the Papagayo jet exit, the upward motion weakened significantly, and the top-heavy profile also diminished. To investigate the possible reasons for changes in the vertical motion profile, we next analyzed the environmental conditions.

Figures 11a–11d show the time mean distribution of the precipitation, MFLUXDIF, sea surface temperature (SST), and column saturation fraction (defined as the ratio of precipitable water to saturated precipitable water) for EW1 and EW2. For EW1, the precipitation is mainly distributed over the Panama Bight and the ocean southwest of Costa Rica and south of Mexico. The zonal rainband near 8–9°N extends to the west, similar to the climatological summertime east Pacific ITCZ rainband. However, precipitation in the Papagayo jet region and its westward extension is very weak, and this dry hole near the Costa Rica Dome has also been documented in previous studies (Rydbeck et al., 2017; Xie et al., 2005). Top-heavy vertical motion represented by positive MFLUXDIF is mainly located over the Panama Bight and the ocean to the west, but is also weak in the jet region. EW2 shows stronger precipitation and top-heavy vertical motion in the Caribbean, but also weak values in the jet region. The above results suggest that weak convection and upward motion in the jet region could be influenced by unfavorable environmental conditions.

The warm SST lies north of 5°N in the east Pacific, with a weaker gradient (Figures 11e and 11f). A cold wedge occurs around 9°N, 91°W west of the jet exit. Xie et al. (2005) indicated that this SST cold spot is due to the shallow thermocline induced by Ekman upwelling in the region of cyclonic shear associated with the Papagayo jet. Its impact on convection is most effective in summer when the ITCZ shifts northward, aligning with the cold SST in this region. This leads to the formation of a dry hole near the Costa Rica Dome within the ITCZ. Large values of saturation fraction are mainly located within the ITCZ (Figures 11g and 11h). For EW1, the maximum moisture is located over the Panama Bight and weakens in the region of the jet. For EW2, on average, the moisture in the Caribbean and the jet region is comparable to that in the Panama Bight.

To further explore the environmental conditions during the disturbance propagation, Figure 12 shows time series of MFLUXDIF, SST, saturation fraction, and instability index averaged over different ranges near the vorticity centers for EW1 and EW2. The instability index used here was introduced by Raymond et al. (2011) and is defined as the difference between the saturated moist entropy averaged in the lower layers (1–3 km) and upper layers (5–7 km). This index represents the moist convective instability in the lower troposphere, and has been shown to be an effective measure regulating convection properties (e.g., Fuchs-Stone et al., 2020; Raymond & Fuchs-Stone, 2021).

MFLUXDIF exhibits some sensitivity to the averaging region, particularly during the early MCS stage, where the results averaged over a 1° × 1° box show stronger amplitude oscillations. However, MFLUXDIF for EW1 and EW2 is generally positive and consistent with the presence of top-heavy vertical motion shown in Figures 6a and 6c, which weakened upon EW formation and then strengthened again after the EW exited the jet region.

The SST in EW1 was lower during the early MCS stage, but increased as the disturbance propagated northwestward. Around 12 UTC on August 8, a significant SST decrease occurred immediately after EW formation, suggesting the vorticity center transited the cold SST wedge, consistent with the results in Figure 11. The SST in EW2 also showed a decrease starting about the time of EW formation in the jet region. Previous studies suggest that high SST generally favors top-heavy vertical motion while cold SST is more likely to induce more bottom-

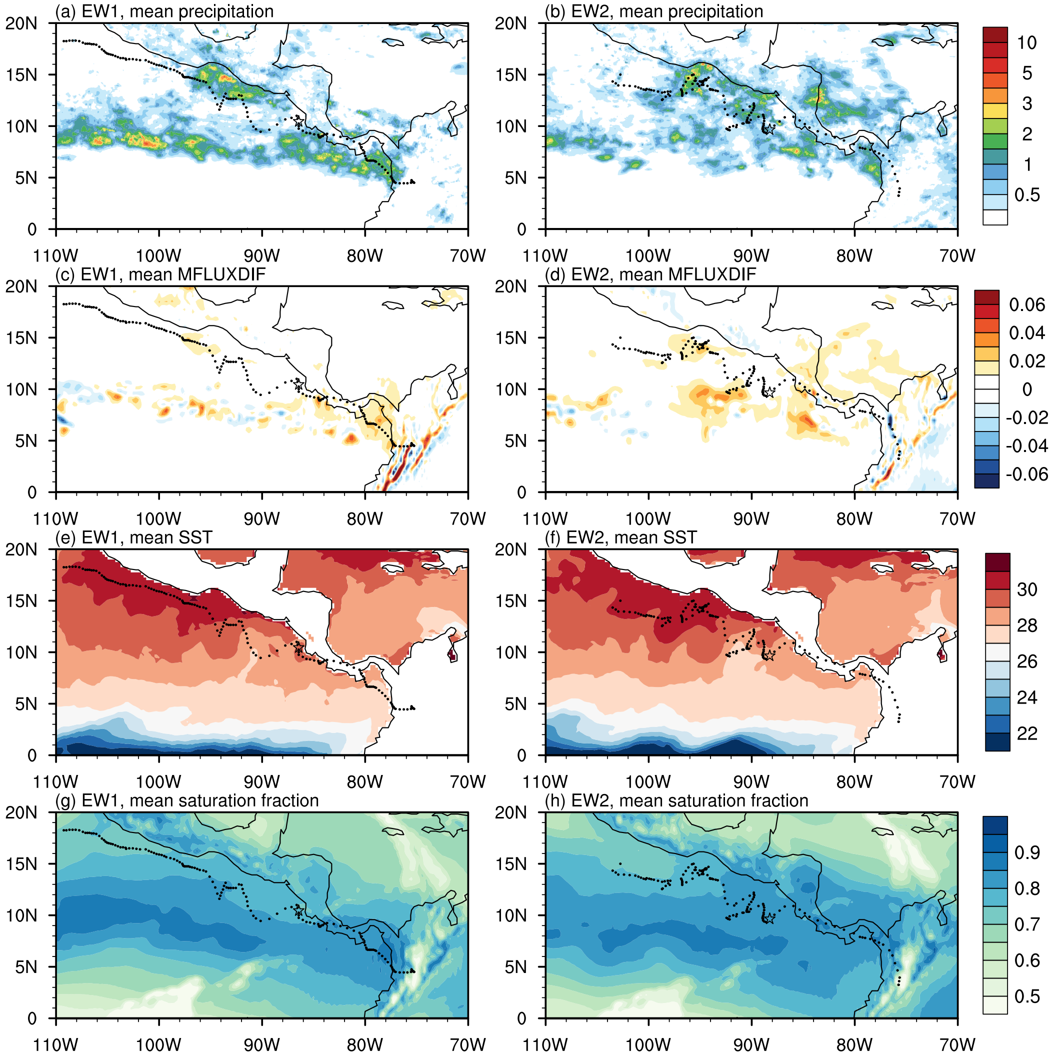

Figure 11. (a) IMERG precipitation rate (mm h^{-1}), (c) ERA5 MFLUXDIF (kg m^{-2} s^{-1}), (e) sea surface temperature (°C), and (g) saturation fraction for EW1 averaged during 6–9 August. (b), (d), (f), And (h) are same as in panels (a), (c), (e), and (g), respectively, but for EW2 averaged during 15–18 August. The black dots denote the 1-hourly vorticity maximum locations for EW1 and EW2, same as in the red dots in Figures 4a and 4b.

heavy structure (Back & Bretherton, 2006; Inoue & Back, 2015; Raymond et al., 2009, 2015). Raymond and Fuchs-Stone (2021) further indicated that while high SST allows but not guarantees a top-heavy profile, low SST almost always results in a bottom-heavy profile. Therefore, the weakened and less top-heavy vertical motion after the formation of EW1 and EW2 is likely to be partly induced by the cold SST. It is worth noting that as the EWs propagated away from the jet region, the SST significantly increased, which may be the main reason for the subsequent enhancement of top-heavy vertical motion and reestablishment of midlevel vorticity (also see Figure 6).

The saturation fraction in EW1 and EW2 intensified after MCS formation to values primarily between 0.85 and 0.9. During the late MCS stage, however, a significant decrease of moisture occurred just before EW formation, likely contributing to inhibited convection. Raymond and Fuchs-Stone (2021) indicated that convection typically occurs within the range of 10–30 J K^{-1} kg^{-1}. For EW1 and EW2, a strong instability index (~20 J K^{-1} kg^{-1}) was observed during the MCS stage consistent with the top-heavy vertical motion, but significantly weakened (<10 J K^{-1} kg^{-1}) after EW formation, consistent with conditions unfavorable for strong convection and top-heavy profiles. Although a positive correlation is found between the instability index and MFLUXDIF, their

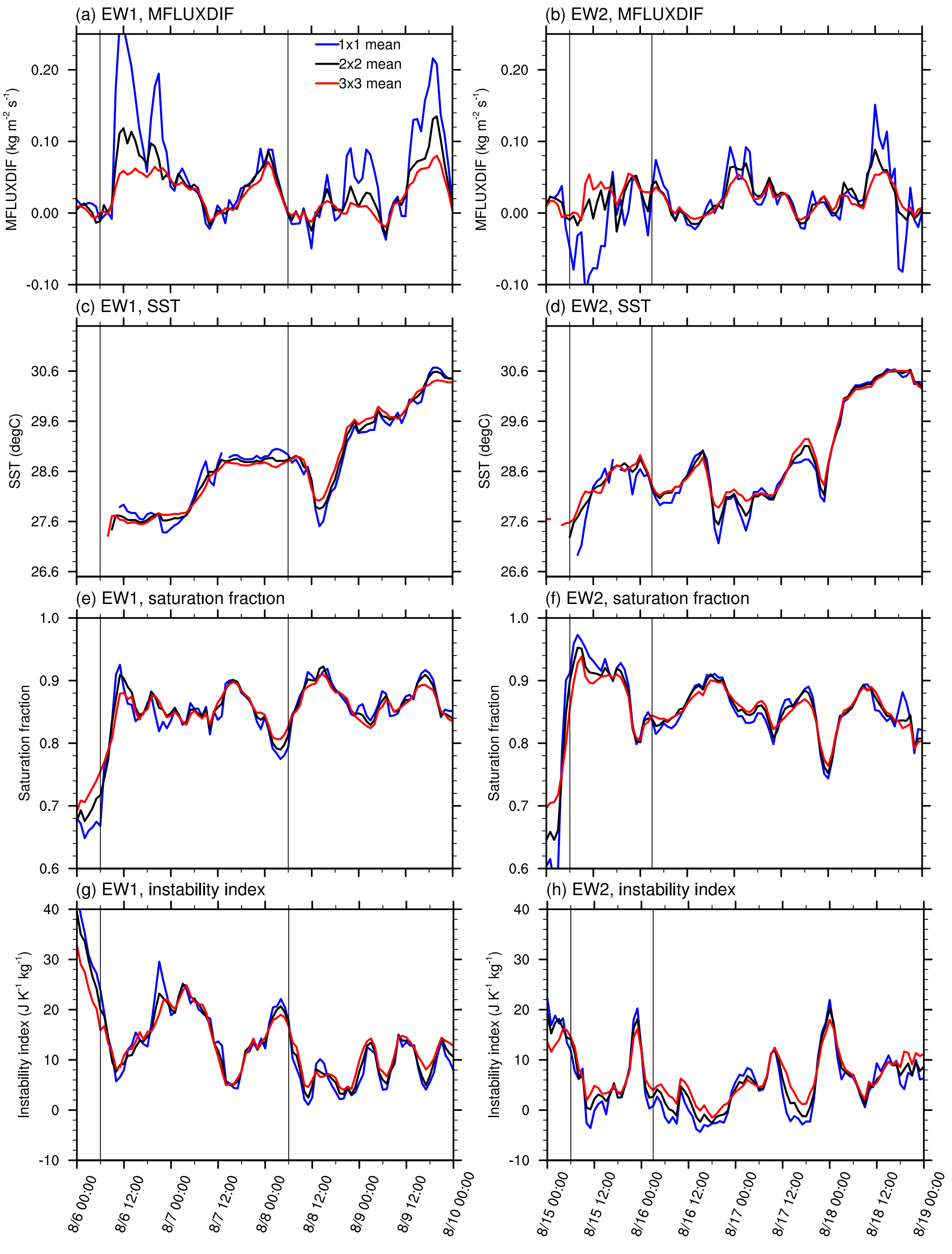

Figure 12. Time series of (a) ERA5 MFLUXDIF (kg m^{-2} s^{-1}), (c) sea surface temperature (°C), (e) saturation fraction, and (g) instability index (J K^{-1} kg^{-1}) averaged across a 1° × 1° (blue), 2° × 2° (black), and 3° × 3° (red) box centered on the 1-hourly 500-hPa vorticity maximum locations for EW1. (b), (d), (f), And (h) are same as in panels (a), (c), (e), and (g), respectively, but for EW2 results averaged near 600-hPa vorticity maximum locations.

correlation coefficients and statistical significance depend strongly on the averaging region. This might be partly due to the noisy distribution of MFLUXDIF, suggesting that it is controlled by multiple factors.

In summary, we suggest that the weak and less top-heavy upward motion near the Papagayo jet is likely influenced jointly by multiple environmental conditions including lower SST, reduced moisture, and weaker convective instability. Because the vertical motion profile significantly affects the vorticity and energy evolution of EWs, further research is needed to identify the key factors and detailed processes modulating its changes.

8. Summary and Discussion

EWs are one of the most important convective systems in the tropical east Pacific. The structure and evolution of vertical motion in EWs play a crucial role in their vorticity growth and interactions with the background jets in the east Pacific, yet these processes are not fully understood. Based on the EW events identified during the OTREC field campaign by Huaman et al. (2021), this study uses satellite, reanalysis, and field observations to study the development of two east Pacific EWs in August 2019. We focus primarily on the vertical motion profile and the associated evolution of vorticity and EKE for the disturbances during their transition from MCSs to EWs. We also explore the environmental factors that may influence the vertical motion profile.

The initial MCS disturbances that seeded EW1 and EW2 formed in the Panama Bight around 06 UTC on August 6 and 15, respectively. The EW1 disturbance propagated smoothly along the Central American coast and developed into an EW near the Papagayo jet exit region around 06 UTC on August 8. The EW2 disturbance merged with other westward-propagating disturbances from the north and the west during its development and evolved into an EW around 03 UTC on August 16.

The disturbances of EW1 and EW2 both exhibited top-heavy upward motion near the midlevel vorticity centers in the MCS stage. When the EW1 disturbance propagated to the south of Papagayo jet, the low-level shear vorticity induced by the strong meridional gradient of zonal wind in that region interacted with the low-level upward motion southwest of the system, enhancing lower tropospheric stretching and vorticity there. Subsequently, top-heavy upward motion strengthened and associated vertical stretching supported midlevel vorticity intensification on the southwest side. This favored the southwest-northeast tilted midlevel vorticity shape and the formation of EW near the Papagayo jet exit. For EW2, the low-level shear vorticity was located further north, and the strong top-heavy motion and related stretching strengthened the midlevel vorticity in the southwest part of the disturbance and led to the formation of EW's tilted feature.

An EKE budget analysis indicates that the strong upper-level EAPE generation and conversion to EKE are associated with diabatic heating induced by top-heavy convection in the Panama Bight and the ocean to the west, serving as the main energy source for development of disturbances in the MCS stage. Barotropic conversion is important in the low levels of Papagayo jet exit, in a region of strong meridional gradient of the zonal wind, which acts as the main energy source near the time of EWs formation. After EW1 and EW2 formed, their upward motion markedly weakened and showed a less top-heavy profile, accompanied by a weakening of midlevel vorticity. Cold SST, lower moisture, and reduced low-level moist convective instability near the jet exit are likely unfavorable for the convection and inhibited the upward motion and precipitation there. The low-level vorticity enhanced by the previous low-level interaction with the jet remained strong after the EWs formation.

Although there are some differences in the propagation and development of EW1 and EW2, the vertical structure evolution of their vertical motion, vorticity, and EKE shows similarities, indicating that the results in this study may be representative of some east Pacific EWs. Whitaker and Maloney (2020) also showed top-heavy vertical motion of MCS disturbance in their EW case in June 2012, which weakened after EW formation and exhibited strong low-level vorticity in the reanalysis, consistent with our findings. However, their WRF simulation did not show this evolution. Instead, it maintained strong midlevel vorticity and weak low-level vorticity. The more top-heavy feature and weaker interaction with the jet in the model may be related to physical parameterization schemes and/or background state biases near the jet exit region, and the specific causes warrant future investigation.

While the enhanced top-heavy vertical motion is directly responsible for the strengthening and tilting of midlevel vorticity and EW formation, the Papagayo jet and related wind shear are important for the earlier occurrence of enhanced stretching and vorticity at low levels, which may alter the later spatial structure of the midlevel vorticity. Additionally, many previous studies suggest that the Papagayo jet induces strong barotropic conversion that may also play a role in EW formation near the exit region (e.g., Maloney & Hartmann, 2001; Rydbeck & Maloney, 2014; Serra et al., 2008, 2010; Whitaker & Maloney, 2018). However, it remains unclear how the barotropic conversion specifically affects the formation and/or subsequent evolution of EWs, and this needs to be investigated using numerical simulations and sensitivity experiments in the future.

In summary, this study presents the observed results for two EW cases during OTREC, providing the basis for further modeling studies. Based on the current findings, we are planning to conduct EW case simulations and sensitivity experiments to further explore the impact of the Papagayo jet on EWs development. Better understanding the mechanisms of east Pacific EWs development may improve our prediction of these disturbances, and may also have implications for predicting the occurrence of tropical cyclones in the east Pacific.

Data Availability Statement

The IMERG precipitation data version 7 (https://disc.gsfc.nasa.gov/datasets/GPM_3IMERGHH_07/summary) are available from the National Aeronautics and Space Administration (NASA). The ERA5 reanalysis data (https://cds.climate.copernicus.eu/) are provided by the European Centre for Medium-Range Weather Forecasts (ECMWF). The flight dropsonde profiles (https://data.eol.ucar.edu/dataset/590.011) and GOES-16 satellite images (https://catalog.eol.ucar.edu/maps/otrec) during the OTREC field campaign are available from the National Center for Atmospheric Research/Earth Observing Laboratory (NCAR/EOL).

Acknowledgments

We thank the two anonymous reviewers for their helpful comments, which improved this manuscript. We acknowledge the funding support from the Climate and Large-Scale Dynamics Program of the National Science Foundation under grant AGS-2217785.

References

Adames, Á. F., & Ming, Y. (2018). Interactions between water vapor and potential vorticity in synoptic-scale monsoonal disturbances: Moisture vortex instability. *Journal of the Atmospheric Sciences*, *75*(6), 2083–2106. https://doi.org/10.1175/JAS-D-17-0310.1

Avila, L. A., & Guiney, J. L. (2000). Eastern North Pacific hurricane season of 1998. *Monthly Weather Review*, *128*(8), 2990–3000. https://doi.org/10.1175/1520-0493(2000)128<2990:ENPHSO>2.0.CO;2

Avila, L. A., & Pasch, R. J. (1992). Atlantic tropical systems of 1991. *Monthly Weather Review*, *120*(11), 2688–2696. https://doi.org/10.1175/1520-0493(1992)120<2688:ATSO>2.0.CO;2

Avila, L. A., Pasch, R. J., Beven, J. L., Franklin, J. L., Lawrence, M. B., Stewart, S. R., & Jiing, J.-G. (2003). Eastern North Pacific hurricane season of 2001. *Monthly Weather Review*, *131*(1), 249–262. https://doi.org/10.1175/1520-0493(2003)131<0249:ASNPHS>2.0.CO;2

Back, L. E., & Bretherton, C. S. (2006). Geographic variability in the export of moist static energy and vertical motion profiles in the tropical Pacific. *Geophysical Research Letters*, *33*(17). https://doi.org/10.1029/2006GL026672

Dominguez, C., Done, J. M., & Bruyère, C. L. (2020). Easterly wave contributions to seasonal rainfall over the tropical Americas in observations and a regional climate model. *Climate Dynamics*, *54*(1–2), 191–209. https://doi.org/10.1007/s00382-019-04996-7

Dunkerton, T. J., Montgomery, M. T., & Wang, Z. (2009). Tropical cyclogenesis in a tropical wave critical layer: Easterly waves. *Atmospheric Chemistry and Physics*, *9*(15), 5587–5646. https://doi.org/10.5194/acp-9-5587-2009

Ferreira, R. N., & Schubert, W. H. (1997). Barotropic aspects of ITCZ breakdown. *Journal of the Atmospheric Sciences*, *54*(2), 261–285. https://doi.org/10.1175/1520-0469(1997)054<0261:BAOIB>2.0.CO;2

Frank, N. L. (1970). Atlantic tropical systems of 1969. *Monthly Weather Review*, *98*(4), 307–314. https://doi.org/10.1175/1520-0493(1970)098<0307:ATSO>2.3.CO;2

Fu, D., Chang, P., Patricola, C. M., Saravanan, R., Liu, X., & Beck, H. E. (2021). Central American mountains inhibit eastern North Pacific seasonal tropical cyclone activity. *Nature Communications*, *12*(1), 4422. https://doi.org/10.1038/s41467-021-24657-w

Fuchs-Stone, Ž., Raymond, D. J., & Sentić, S. (2020). OTREC2019: Convection over the east Pacific and southwest Caribbean. *Geophysical Research Letters*, *47*(11). https://doi.org/10.1029/2020GL087564

Hersbach, H., Bell, B., Berrisford, P., Biavati, G., Horányi, A., Muñoz Sabater, J., et al. (2023). ERA5 hourly data on pressure levels from 1940 to present [Dataset]. *Copernicus Climate Change Service (C3S) Climate Data Store (CDS)*. https://doi.org/10.24381/cds.bd0915c6

Holbach, H. M., & Bourassa, M. A. (2014). The effects of gap-wind-induced vorticity, the monsoon trough, and the ITCZ on east Pacific tropical cyclogenesis. *Monthly Weather Review*, *142*(3), 1312–1325. https://doi.org/10.1175/MWR-D-13-00218.1

Huaman, L., Maloney, E. D., Schumacher, C., & Kiladis, G. N. (2021). Easterly waves in the east Pacific during the OTREC 2019 field campaign. *Journal of the Atmospheric Sciences*, *78*(12), 4071–4088. https://doi.org/10.1175/JAS-D-21-0128.1

Huffman, G. J., Stocker, E. F., Bolvin, D. T., Nelkin, E. J., & Jackson, T. (2023). GPM IMERG final precipitation L3 half hourly 0.1 degree x 0.1 degree V07 [Dataset]. *Goddard Earth Sciences Data and Information Services Center (GES DISC)*. https://doi.org/10.5067/GPM/IMERG/3B-HH/07

Inoue, K., & Back, L. E. (2015). Gross moist stability assessment during TOGA COARE: Various interpretations of gross moist stability. *Journal of the Atmospheric Sciences*, *72*(11), 4148–4166. https://doi.org/10.1175/JAS-D-15-0092.1

Jaramillo, L., Poveda, G., & Mejía, J. F. (2017). Mesoscale convective systems and other precipitation features over the tropical Americas and surrounding seas as seen by TRMM. *International Journal of Climatology*, *37*(S1), 380–397. https://doi.org/10.1002/joc.5009

Lau, K.-H., & Lau, N.-C. (1992). The energetics and propagation dynamics of tropical summertime synoptic-scale disturbances. *Monthly Weather Review*, *120*(11), 2523–2539. https://doi.org/10.1175/1520-0493(1992)120<2523:TEAPDO>2.0.CO;2

Maloney, E. D., & Hartmann, D. L. (2001). The Madden–Julian oscillation, barotropic dynamics, and North Pacific tropical cyclone formation. Part I: Observations. *Journal of the Atmospheric Sciences*, *58*(17), 2545–2558. https://doi.org/10.1175/1520-0469(2001)058<2545:TMJOBD>2.0.CO;2

Mapes, B. E., Warner, T. T., Xu, M., & Negri, A. J. (2003). Diurnal patterns of rainfall in northwestern South America. Part I: Observations and context. *Monthly Weather Review*, *131*(5), 799–812. https://doi.org/10.1175/1520-0493(2003)131<0799:DPORIN>2.0.CO;2

Mejía, J. F., Yepes, J., Henao, J. J., Poveda, G., Zuluaga, M. D., Raymond, D. J., & Fuchs-Stone, Ž. (2021). Towards a mechanistic understanding of precipitation over the far eastern tropical Pacific and western Colombia, one of the rainiest spots on Earth. *Journal of Geophysical Research: Atmospheres*, *126*(5). https://doi.org/10.1029/2020JD033415

Molinari, J., & Vollaro, D. (2000). Planetary- and synoptic-scale influences on eastern Pacific tropical cyclogenesis. *Monthly Weather Review*, *128*(9), 3296–3307. https://doi.org/10.1175/1520-0493(2000)128<3296:PASSIO>2.0.CO;2

Nitta, T., & Takayabu, Y. (1985). Global analysis of the lower tropospheric disturbances in the tropics during the northern summer of the FGGE year part II: Regional characteristics of the disturbances. *Pure and Applied Geophysics PAGEOPH*, *123*(2), 272–292. https://doi.org/10.1007/BF00877023

Pasch, R. J., Blake, E. S., Avila, L. A., Beven, J. L., Brown, D. P., Franklin, J. L., et al. (2009). Eastern North Pacific hurricane season of 2006. *Monthly Weather Review*, *137*(1), 3–20. https://doi.org/10.1175/2008MWR2508.1

Rappaport, E. N., & Mayfield, M. (1992). Eastern North Pacific hurricane season of 1991. *Monthly Weather Review*, *120*(11), 2697–2708. https://doi.org/10.1175/1520-0493(1992)120<2697:ENPHSO>2.0.CO;2

Raymond, D. J., & Fuchs-Stone, Ž. (2021). Emergent properties of convection in OTREC and PREDICT. *Journal of Geophysical Research: Atmospheres*, *126*(4). https://doi.org/10.1029/2020JD033585

Raymond, D. J., Fuchs-Stone, Ž., Gjorgjievska, S., & Sessions, S. (2015). Balanced dynamics and convection in the tropical troposphere. *Journal of Advances in Modeling Earth Systems*, *7*(3), 1093–1116. https://doi.org/10.1002/2015MS000467

Raymond, D. J., Sessions, S. L., & López Carrillo, C. (2011). Thermodynamics of tropical cyclogenesis in the northwest Pacific. *Journal of Geophysical Research*, *116*(D18), D18101. https://doi.org/10.1029/2011JD015624

Raymond, D. J., Sessions, S. L., Sobel, A. H., & Fuchs, Ž. (2009). The mechanics of gross moist stability. *Journal of Advances in Modeling Earth Systems*, *1*(3). https://doi.org/10.3894/JAMES.2009.1.9

Roundy, P. E., & Frank, W. M. (2004). A climatology of waves in the equatorial region. *Journal of the Atmospheric Sciences*, *61*(17), 2105–2132. https://doi.org/10.1175/1520-0469(2004)061<2105:ACOWIT>2.0.CO;2

Rydbeck, A. V., & Maloney, E. D. (2014). Energetics of east Pacific easterly waves during intraseasonal events. *Journal of Climate*, *27*(20), 7603–7621. https://doi.org/10.1175/JCLI-D-14-00211.1

Rydbeck, A. V., & Maloney, E. D. (2015). On the convective coupling and moisture organization of east Pacific easterly waves. *Journal of the Atmospheric Sciences*, *72*(10), 3850–3870. https://doi.org/10.1175/JAS-D-15-0056.1

Rydbeck, A. V., Maloney, E. D., & Alaka, G. J. (2017). In situ initiation of east Pacific easterly waves in a regional model. *Journal of the Atmospheric Sciences*, *74*(2), 333–351. https://doi.org/10.1175/JAS-D-16-0124.1

Serra, Y. L., Kiladis, G. N., & Cronin, M. F. (2008). Horizontal and vertical structure of easterly waves in the Pacific ITCZ. *Journal of the Atmospheric Sciences*, *65*(4), 1266–1284. https://doi.org/10.1175/2007JAS2341.1

Serra, Y. L., Kiladis, G. N., & Hodges, K. I. (2010). Tracking and mean structure of easterly waves over the Intra-Americas Sea. *Journal of Climate*, *23*(18), 4823–4840. https://doi.org/10.1175/2010JCLI3223.1

Shapiro, L. J. (1986). The three-dimensional structure of synoptic-scale disturbances over the tropical Atlantic. *Monthly Weather Review*, *114*(10), 1876–1891. https://doi.org/10.1175/1520-0493(1986)114<1876:TTDSOS>2.0.CO;2

Tai, K.-S., & Ogura, Y. (1987). An observational study of easterly waves over the eastern Pacific in the northern summer using FGGE data. *Journal of the Atmospheric Sciences*, *44*(2), 339–361. https://doi.org/10.1175/1520-0469(1987)044<0339:AOSOEW>2.0.CO;2

Toma, V. E., & Webster, P. J. (2010a). Oscillations of the intertropical convergence zone and the genesis of easterly waves. Part I: Diagnostics and theory. *Climate Dynamics*, *34*(4), 587–604. https://doi.org/10.1007/s00382-009-0584-x

Toma, V. E., & Webster, P. J. (2010b). Oscillations of the Intertropical Convergence Zone and the genesis of easterly waves Part II: Numerical verification. *Climate Dynamics*, *34*(4), 605–613. https://doi.org/10.1007/s00382-009-0585-9

Torres, V. M., Thorncroft, C. D., & Hall, N. M. J. (2021). Genesis of easterly waves over the tropical eastern Pacific and the Intra-Americas Sea. *Journal of the Atmospheric Sciences*, *78*(10), 3263–3279. https://doi.org/10.1175/JAS-D-20-0389.1

Valencia, J., Yepes, J., Mejía, J. F., Builes-Jaramillo, A., & Salas, H. D. (2024). Influence of tropical easterly waves on the ChocoJet during the 2019 OTREC campaign. *Journal of Hydrometeorology*, *25*(2), 325–337. https://doi.org/10.1175/JHM-D-23-0039.1

Vömel, H. (2019). NCAR/EOL AVAPS dropsonde QC data Version 1.0 [Dataset]. *UCAR/NCAR - Earth Observing Laboratory*. https://doi.org/10.26023/EHRT-TN96-9W04

Vömel, H., Goodstein, M., Tudor, L., Witte, J., Fuchs-Stone, Ž., Sentić, S., et al. (2021). High-resolution in situ observations of atmospheric thermodynamics using dropsondes during the Organization of Tropical East Pacific Convection (OTREC) field campaign. *Earth System Science Data*, *13*(3), 1107–1117. https://doi.org/10.5194/essd-13-1107-2021

Whitaker, J. W., & Maloney, E. D. (2018). Influence of the Madden–Julian oscillation and Caribbean low-level jet on east Pacific easterly wave dynamics. *Journal of the Atmospheric Sciences*, *75*(4), 1121–1141. https://doi.org/10.1175/JAS-D-17-0250.1

Whitaker, J. W., & Maloney, E. D. (2020). Genesis of an east Pacific easterly wave from a Panama Bight MCS: A case study analysis from June 2012. *Journal of the Atmospheric Sciences*, *77*(10), 3567–3584. https://doi.org/10.1175/JAS-D-20-0032.1

Wiggins, R. M., Lintner, B. R., Serra, Y. L., Durán-Quesada, A. M., Garbanzo-Salas, M., Hernández-Deckers, D., & Torri, G. (2023). Tropical easterly waves over Costa Rica and their relationship to the diurnal cycle of rainfall. *Geophysical Research Letters*, *50*(20). https://doi.org/10.1029/2023GL104159

Xie, S.-P., Xu, H., Kessler, W. S., & Nonaka, M. (2005). Air–sea interaction over the eastern Pacific warm pool: Gap winds, thermocline dome, and atmospheric convection. *Journal of Climate*, *18*(1), 5–20. https://doi.org/10.1175/JCLI-3249.1

Zehnder, J. A., Powell, D. M., & Ropp, D. L. (1999). The interaction of easterly waves, orography, and the intertropical convergence zone in the genesis of eastern Pacific tropical cyclones. *Monthly Weather Review*, *127*(7), 1566–1585. https://doi.org/10.1175/1520-0493(1999)127<1566:TIOEWO>2.0.CO;2